Monthly Notices of the ROYAL ASTRONOMICAL SOCIETY

MNRAS **467,** 540–572 (2017)
Advance Access publication 2017 January 11

doi:10.1093/mnras/stx055

BAT AGN Spectroscopic Survey – IV. Near-infrared coronal lines, hidden broad lines and correlation with hard X-ray emission

Isabella Lamperti,[1]★ Michael Koss,[1,2]† Benny Trakhtenbrot,[1]‡ Kevin Schawinski,[1] Claudio Ricci,[3] Kyuseok Oh,[1] Hermine Landt,[4] Rogério Riffel,[5] Alberto Rodríguez-Ardila,[6] Neil Gehrels,[7] Fiona Harrison,[8] Nicola Masetti,[9,10] Richard Mushotzky,[11] Ezequiel Treister,[3] Yoshihiro Ueda[12] and Sylvain Veilleux[11]

[1]*Institute for Astronomy, Department of Physics, ETH Zurich, Wolfgang-Pauli-Strasse 27, CH-8093 Zürich, Switzerland*
[2]*Institute for Astronomy, University of Hawaii, 2680 Woodlawn Drive, Honolulu, HI 96822, USA*
[3]*Instituto de Astrofísica, Facultad de Física, Pontificia Universidad Católica de Chile, Casilla 306, Santiago 22, Chile*
[4]*Centre for Extragalactic Astronomy, Department of Physics, Durham University, South Road, Durham DH1 3LE, UK*
[5]*Departamento de Astronomia, Universidade Federal do Rio Grande do Sul., Av. Bento Gonçalves 9500, Porto Alegre, RS, Brazil*
[6]*Laboratφrio Nacional de Astrofísica, Rua dos Estados Unidos 154, Bairro das Nações, CEP 37504-364 Itajubá, MG, Brazil*
[7]*NASA Goddard Space Flight Center, Greenbelt, MD 20771, USA*
[8]*Cahill Center for Astronomy and Astrophysics, California Institute of Technology, Pasadena, CA 91125, USA*
[9]*INAF – Istituto di Astrofisica Spaziale e Fisica Cosmica di Bologna, via Gobetti 101, I-40129 Bologna, Italy*
[10]*Departamento de Ciencias Físicas, Universidad Andrés Bello, Fernández Concha 700, Las Condes, Santiago, Chile*
[11]*Department of Astronomy and Joint Space-Science Institute, University of Maryland, College Park, MD 20742, USA*
[12]*Department of Astronomy, Kyoto University, Kyoto 606-8502, Japan*

Accepted 2017 January 9. Received 2017 January 9; in original form 2016 September 30

ABSTRACT

We provide a comprehensive census of the near-infrared (NIR, 0.8–2.4 μm) spectroscopic properties of 102 nearby ($z < 0.075$) active galactic nuclei (AGN), selected in the hard X-ray band (14–195 keV) from the *Swift*-Burst Alert Telescope survey. With the launch of the *James Webb Space Telescope*, this regime is of increasing importance for dusty and obscured AGN surveys. We measure black hole masses in 68 per cent (69/102) of the sample using broad emission lines (34/102) and/or the velocity dispersion of the Ca II triplet or the CO band-heads (46/102). We find that emission-line diagnostics in the NIR are ineffective at identifying bright, nearby AGN galaxies because [Fe II] 1.257 μm/Paβ and H_2 2.12 μm/Brγ identify only 25 per cent (25/102) as AGN with significant overlap with star-forming galaxies and only 20 per cent of Seyfert 2 have detected coronal lines (6/30). We measure the coronal line emission in Seyfert 2 to be weaker than in Seyfert 1 of the same bolometric luminosity suggesting obscuration by the nuclear torus. We find that the correlation between the hard X-ray and the [Si VI] coronal line luminosity is significantly better than with the [O III] λ5007 luminosity. Finally, we find 3/29 galaxies (10 per cent) that are optically classified as Seyfert 2 show broad emission lines in the NIR. These AGN have the lowest levels of obscuration among the Seyfert 2s in our sample ($\log N_H < 22.43$ cm^{-2}), and all show signs of galaxy-scale interactions or mergers suggesting that the optical broad emission lines are obscured by host galaxy dust.

Key words: galaxies: active – quasars: emission lines – quasars: general – galaxies: Seyfert – infrared: galaxies – X-rays: galaxies.

1 INTRODUCTION

The near-infrared (NIR) spectral regime (0.8–2.4 μm) provides numerous emission lines for studies of active galactic nuclei (AGN) and has the advantage to be 10 times less obscured than the optical (Veilleux 2002). For example, the vibrational and rotational

★ E-mail: lamperis@phys.ethz.ch
† Ambizione Fellow.
‡ Zwicky Fellow.

modes of H_2 can be excited by UV fluorescence (Black & van Dishoeck 1987; Rodríguez-Ardila et al. 2004; Rodríguez-Ardila, Riffel & Pastoriza 2005; Riffel et al. 2013), shock heating (Hollenbach & McKee 1989) and heating by X-rays, where hard X-ray photons penetrate into molecular clouds and heat the molecular gas (Maloney, Hollenbach & Tielens 1996). The [Fe II] emission in AGN can be produced by shocks from the radio jets or X-ray heating, while in star-forming galaxies (SFGs) the [Fe II] emission is produced by photoionization or supernovae shocks (Rodríguez-Ardila et al. 2004).

NIR emission-line diagnostics (e.g. Larkin et al. 1998; Rodríguez-Ardila et al. 2004; Riffel et al. 2013; Colina et al. 2015) are based on the close relation between the line ratios [Fe II] 1.257 μm/Paβ and H_2 2.12 μm/Brγ, and the nuclear black hole activity. In principle, the low levels of dust attenuation in the NIR imply that such line diagnostics can be used even among highly reddened objects. However, several studies (e.g. Dale et al. 2004; Martins et al. 2013) found that this diagnostic is not effective in separating SFGs from AGN.

The NIR regime also includes the hydrogen Paα and Paβ emission lines, which by virtue of being less obscured may at times (∼30 per cent of sources) present a 'hidden' broad-line region (BLR), in galaxies with narrow optical Hβ and/or Hα lines (e.g. Veilleux, Goodrich & Hill 1997; Onori et al. 2014; Smith, Koss & Mushotzky 2014; La Franca et al. 2015). Onori et al. (2016) recently studied a sample of 41 obscured (Sy2) and intermediate-class AGN (Sy1.8–1.9) and found broad Paα, Paβ or He I lines in 32 per cent (13/41) of the sources. The study of Landt et al. (2008) compared the width of the Paschen and Balmer lines (in terms of full width at half-maximum – FWHM) and found that Hβ is generally broader than Paβ. One possible reason for this trend is the presence of the Hβ 'red shelf' (e.g. De Robertis 1985; Marziani et al. 1996), which originates from Fe II multiplets (Veron, Goncalves & Veron-Cetty 2002). Another possibility is that the broad Balmer lines originate from a region closer to the black hole than the Paschen lines (Kim, Im & Kim 2010).

The NIR broad Paschen emission lines can be used to derive black hole mass ($M_{\rm BH}$) estimates, based on their luminosities and widths, following a similar approach to that based on the optical Balmer lines (e.g. Kim et al. 2010; Landt et al. 2011b, 2013). Alternatively, the size of the BLR ($R_{\rm BLR}$), and therefore $M_{\rm BH}$, can also be estimated using the 1-μm continuum luminosity (Landt et al. 2011a) or the hard-band X-ray luminosity (e.g. La Franca et al. 2015), again mimicking similar methods to those put forward for the Balmer lines (Greene et al. 2010). For obscured AGN, the spectral region surrounding the Ca II triplet of absorption features (0.845–0.895 μm; e.g. Rothberg & Fischer 2010; Rothberg et al. 2013) and CO bandheads in the *H* and *K* band (e.g. Dasyra et al. 2006a,b, 2007; Kang et al. 2013; Riffel et al. 2015) are useful regions to measure the stellar velocity dispersion (σ_*) to infer $M_{\rm BH}$ following the $M_{\rm BH}$–σ_* relation (Ferrarese & Merritt 2000; Tremaine et al. 2002; McConnell & Ma 2012; Kormendy & Ho 2013).

Moreover, the NIR regime is important because it includes several high-ionization (>100 eV) coronal lines (CLs) generated through photoionization by the hard UV and soft X-ray continuum produced by AGN or by shocks (e.g. Rodríguez-Ardila et al. 2002, 2011). CLs tend to be broader than low-ionization emission lines emitted in the narrow line region (NLR), but narrower than lines in the BLR (400 km s^{-1} < FWHM < 1000 km s^{-1}). This suggests that they are produced in a region between the BLR and the NLR (Rodríguez-Ardila et al. 2006). Müller-Sánchez et al. (2011) investigated the spatial distribution of CLs and found that the size of the coronal line region (CLR) only extends to a distances of <200 pc from the centre of the galaxy (Mazzalay, Rodríguez-Ardila & Komossa 2010; Müller-Sánchez et al. 2011).

Recently, it has been found that high-ionization optical emission lines, such as [O III] λ5007, are only weakly correlated with AGN X-ray luminosity or with bolometric luminosity (Berney et al. 2015; Ueda et al. 2015). The considerable intrinsic scatter in this relation (0.6 dex) may be related to physical properties of the NLR such as covering factor of the NLR (e.g. Netzer & Laor 1993), density dependence of [O III] (Crenshaw & Kraemer 2005), differing ionization parameter (Baskin & Laor 2005) and spectral energy distribution (SED) shape changes with luminosity (Netzer et al. 2006). Other possible reasons are AGN variability (Schawinski et al. 2015), dust obscuration, or contamination from star formation. CLs in the NIR, by virtue of the higher ionization potentials (IPs) and the minor sensitivity to dust obscuration, provide an additional method to study this correlation.

In this work, we aim to study the NIR properties of one of the largest samples of nearby AGN (102) from the *Swift*/Burst Alert Telescope (BAT) survey selected at 14–195 keV (Baumgartner et al. 2013) as part of the BAT AGN Spectroscopic Survey (BASS). This sample, by virtue of its selection, is nearly unbiased to obscuration up to Compton-thick levels (Koss et al. 2016). The first BASS paper (Koss et al., submitted) detailed the optical spectroscopic data and measurements. The second BASS paper (Berney et al. 2015) studied the large scatter in X-rays and high-ionization emission lines like [O III]. Additionally, all of the AGN have been analysed using X-ray observations including the best available soft X-ray data in the 0.3–10-keV band from *XMM-Newton*, *Chandra*, *Suzaku*or *Swift*/XRT and the 14–195 keV band from *Swift*/BAT, which provide measurements of the obscuring column density ($N_{\rm H}$; Ricci et al. 2015, submitted). Therefore, we are able to compare the NIR properties of these AGN with their optical and X-ray characteristics, to better understand AGN variability and obscuration. Throughout this work, we use a cosmological model with $\Omega_\Lambda = 0.7$, $\Omega_{\rm M} = 0.3$ and $H_0 = 70$ km s^{-1} Mpc^{-1} to determine distances. However, for the most nearby sources in our sample ($z < 0.01$), we use the mean of the redshift-independent distance in Mpc from the NASA/IPAC Extragalactic Database (NED), whenever available.

2 DATA AND REDUCTION

2.1 Sample

The *Swift*/BAT observatory carried out an all-sky survey in the ultrahard X-ray range (>10 keV) that, as of the first 70 months of operation, has identified 1210 objects (Baumgartner et al. 2013) of which 836 are AGN. The majority (≈90 per cent) of BAT-detected AGN are relatively nearby ($z < 0.2$).

We limited our NIR spectra sample to 102 nearby AGN with redshift $z < 0.075$ to ensure high-quality observations for both Seyfert 1 and Seyfert 2. In our sample, there are 69 Seyfert 1 and 33 Seyfert 2. A full list of the AGN can be found in Tables 1–3. Fig. 1 shows the distribution of the hard X-ray luminosity of the AGN in our sample as a function of redshift. Most of the AGN (96) are listed in the *Swift*/BAT 70-month catalogue (Baumgartner et al. 2013) with an additional six AGN from the Palermo 100-month BAT catalogue (Cusumano et al. 2010) and the upcoming *Swift*/BAT 104-month catalogue (Oh et al., in preparation).

The goal of our survey was to use the largest available NIR spectroscopic sample of *Swift*/BAT sources using dedicated observations and published data. More than half (55 per cent, 56/102) of the AGN

Table 1. Spectra from the IRTF observations.

ID[a]	Counterpart name	Redshift	Slit size (arcsec)	Slit size (kpc)	Date (yy-mm-dd)	Air mass	Exp. time (s)	Type[b]	H[c] (mag)
316	IRAS 05589+2828	0.033	0.8	0.54	11-04-12	1.23	2160	1.2	–
399	2MASX J07595347+2323241	0.0292	0.8	0.48	12-03-14	1.01	2160	1.9	10.3
434	MCG +11-11-032	0.036	0.8	0.59	12-03-14	1.42	2160	2	11.4
439	Mrk 18	0.0111	0.8	0.18	11-04-12	1.33	2520	1.9	10.5
451	IC 2461	0.0075	0.8	0.13	12-03-14	1.11	1080	2	10.1
515	MCG +06-24-008	0.0259	0.8	0.43	12-03-19	1.12	2520	2	10.8
517	UGC 05881	0.0205	0.8	0.34	11-04-12	1.01	1800	2	10.9
533	NGC 3588 NED01	0.0268	0.8	0.44	11-04-12	1.02	1620	2	10.6
548	NGC 3718	0.0033	0.8	0.05	10-06-11	1.24	4140	1.9	7.9
586	ARK 347	0.0224	0.8	0.37	12-03-19	1.17	2520	2	10.7
588	UGC 7064	0.025	0.8	0.41	12-03-19	1.58	2340	1.9	10.3
590	NGC 4102	0.0028	0.8	0.05	10-06-11	1.26	1200	2	7.8
592	Mrk 198	0.0242	0.8	0.40	12-03-19	1.16	2520	2	11.2
593	NGC 4138	0.003	0.8	0.05	10-06-11	1.24	3240	2	8.3
635	KUG 1238+278A	0.0565	0.8	0.93	12-03-02	1.07	3600	1.9	11.8
638	NGC 4686	0.0167	0.8	0.28	11-04-12	1.22	3240	2	9.1
659	NGC 4992	0.0251	0.8	0.42	11-04-12	1.04	3960	2	10.3
679	NGC 5231	0.0218	0.8	0.36	10-06-12	1.07	1800	2	10.4
682	NGC 5252	0.023	0.8	0.38	10-06-12	1.12	1800	2	9.9
686	NGC 5273	0.0036	0.8	0.06	10-06-12	1.19	1800	1.5	8.8
687	CGCG 102−048	0.0269	0.8	0.44	12-03-19	1.35	2160	2	11.3
695	UM614	0.0327	0.8	0.54	11-04-12	1.53	1200	1.5	11.6
712	NGC 5506	0.0062	0.8	0.10	10-06-11	1.21	1200	1.9	8.2
723	NGC 5610	0.0169	0.8	0.28	11-04-12	1.02	2520	2	10.1
734	NGC 5683	0.0362	0.8	0.60	12-03-13	1.19	2160	1.2	11.8
737	2MASX J14391186+1415215	0.0714	0.8	1.17	11-04-12	1.08	3420	2	13.1
738	Mrk 477	0.0377	0.8	0.62	11-04-12	1.49	1440	1.9	12.1
748	2MASX J14530794+2554327	0.049	0.8	0.80	10-06-11	1.10	1800	1	12.5
754	Mrk 1392	0.0361	0.8	0.60	11-04-12	1.56	1200	1.5	11.1
783	NGC 5995	0.0252	0.8	0.42	11-06-16	1.24	1800	1.9	9.5
883	2MASX J17232321+3630097	0.04	0.8	0.66	11-06-16	1.04	960	1.5	11.4
1041	2MASS J19334715+3254259	0.0583	0.8	0.96	10-06-11	1.08	1680	1.2	–
1042	2MASX J19373299−0613046	0.0107	0.8	0.18	11-09-14	1.16	720	1.5	9.7
1046	NGC 6814	0.0052	0.8	0.09	11-09-14	1.19	1200	1.5	7.8
1077	MCG +04-48-002	0.0139	0.8	0.23	10-06-12	1.02	1800	2	9.9
1099	2MASX J21090996−0940147	0.0277	0.8	0.46	11-09-14	1.23	1800	1.2	10.6
1106	2MASX J21192912+3332566	0.0507	0.8	0.83	11-09-15	1.04	1800	1.5	11.5
1117	2MASX J21355399+4728217	0.0259	0.8	0.43	10-06-11	1.32	1800	1.5	11.5
1133	Mrk 520	0.0273	0.8	0.45	10-06-12	1.08	1800	2	10.8
1157	NGC 7314	0.0048	0.8	0.08	11-09-15	1.43	1440	1.9	8.3
1158	NGC 7319	0.0225	0.8	0.37	10-06-11	1.28	1800	2	10.4
1161	Mrk 915	0.0241	0.8	0.40	11-09-15	1.2	1440	1.9	10.4
1178	KAZ 320	0.0345	0.8	0.57	10-06-12	1.08	1800	1.5	12.1
1183	Mrk 926	0.0469	0.8	0.77	10-06-11	1.42	1800	1.5	10.8
1196	2MASX J23272195+1524375	0.0465	0.8	0.76	11-09-15	1	1440	1.9	11.1
1202	UGC 12741	0.0174	0.8	0.29	10-06-11	1.15	1200	2	10.8
1472	CGCG 198−020	0.0269	0.8	0.44	10-06-12	1.13	1800	1.5	–
1570	NGC 5940	0.0339	0.8	0.56	10-06-12	1.31	1800	1	–

Notes. [a]*Swift*/BAT 70-month hard X-ray survey ID (http://swift.gsfc.nasa.gov/results/bs70mon/).
[b]AGN classification following Osterbrock (1981).
[c]H 20 mag arcsec^{-2} isophotal fiducial elliptical aperture magnitudes from the 2MASS extended source catalogue.

were observed as part of a targeted campaigns using the SpeX spectrograph (Rayner et al. 2003) at the NASA 3-m Infrared Telescope Facility (IRTF; 49 sources) or with the Florida Multi-object Imaging Near-IR Grism Observational Spectrometer (FLAMINGOS; Elston 1998) on the Kitt Peak 4-m telescope (seven sources). The targets were selected at random based on visibility from the northern sky. Additionally, we included spectra from available archival observations. We used 15 spectra from Riffel, Rodríguez-Ardila & Pastoriza (2006), 14 spectra from Landt et al. (2008), two spectra from Rodríguez-Ardila et al. (2002) and one spectrum from Riffel et al. (2013) observed with IRTF. We used three spectra observed by Landt et al. (2013) and 13 publicly available spectra from Mason et al. (2015) observed with the Gemini Near-Infrared Spectrograph (GNIRS; Elias et al. 2006) on the 8.1-m Gemini North telescope. We note there is some bias towards observing more Seyfert 1 in our sample compared to a blind survey of BAT AGN (≈50 per cent Seyfert 1) because some archival studies focused on Seyfert 1 (e.g. Landt et al. 2008).

Table 2. Spectra from the FLAMINGOS observations.

ID[a]	Counterpart name	Redshift	Slit size (arcsec)	Slit size (kpc)	Date (yy-mm-dd)	Air mass	Exp. time (s)	Type[b]	H[c] (mag)
310	MCG +08-11-011	0.0205	1.5	0.64	08-12-13	1.03	1440	1.5	9.3
325	Mrk 3	0.0135	1.5	0.42	08-12-13	1.29	1440	1.9	9.1
766	NGC 5899	0.0086	1.5	0.27	09-07-07	1.2	1440	2	8.7
772	MCG -01-40-001	0.0227	1.5	0.70	09-07-07	1.37	1440	1.9	10.4
804	CGCG 367-009	0.0274	1.5	0.85	09-07-06	1.6	1440	2	11.3
1040	2MASX J19301380+3410495	0.0629	1.5	1.93	09-07-06	1.46	1440	1.5	–
1177	UGC 12282	0.017	1.5	0.53	09-07-07	1.03	1440	2	9.1

Notes. [a] *Swift*/BAT 70-month hard X-ray survey ID (http://swift.gsfc.nasa.gov/results/bs70mon/).
[b] AGN classification following Osterbrock (1981).
[c] H 20 mag arcsec^{-2} isophotal fiducial elliptical aperture magnitudes from the 2MASS extended source catalogue.

We used the [O III] redshift, optical emission-line measurements and classification in Seyfert 1 and Seyfert 2 from Koss et al. (submitted). Optical counterparts of BAT AGN and the 14–195-keV measurements were based on Baumgartner et al. (2013). We also used the $N_{\rm H}$ and 2–10-keV flux measurements from Ricci et al. (2015, submitted). The optical observations were not taken simultaneously to the NIR observations but come from separate targeted campaigns or public archives.

2.2 NIR spectral data

While the data were taken from a number of observational campaigns, we maintain a uniform approach to data reduction and analysis. The observations were taken in the period 2010–2012. A summary of all the observational set-ups can be found in Table 4. All programs used standard A0V stars with similar air masses to provide a benchmark for telluric correction. The majority of observations were done with the cross-dispersed mode of SpeX on the IRTF using a 0.8 arcsec × 15 arcsec slit (Rayner et al. 2003) covering a wavelength range from 0.8 to 2.4 μm. The galaxies were observed in two positions along the slit, denoted position A and position B, in an ABBA sequence by moving the telescope. This provided pairs of spectra that could be subtracted to remove the sky emission and detector artefacts. For 16 objects, we have duplicate observations. In these cases, we chose the spectrum with the higher signal-to-noise ratio (S/N) in the continuum.

2.2.1 *Targeted spectroscopic observations*

For new observations, the data reduction was performed using standard techniques with SPEXTOOL, a software package developed especially for IRTF SpeX observations (Cushing, Vacca & Rayner 2004). The spectra were tellurically corrected using the method described by Vacca, Cushing & Rayner (2002) and the IDL routine `Xtellcor`, using a Vega model modified by deconvolution with the spectral resolution. The routine `Xcleanspec` was used to remove regions of the spectrum that were completely absorbed by the atmosphere. The spectra were then smoothed using a Savitzky–Golay routine, which preserves the average resolving power. We used the smoothed spectra for the measurements of the emission lines, whereas for the absorption lines' analysis we used the unsmoothed spectra. Further details are provided in Smith et al. (2014) and in the appendix.

We also have seven spectra observed with the FLAMINGOS spectrograph at Kitt Peak over the wavelength range 0.9–2.3 μm using two set-ups, one with the *JH* grism and the other with the *K* grism both using a 1.5-arcsec slit. The spectra were first flat-fielded, wavelength calibrated, extracted and combined using IRAF routines. Then telluric corrections and flux calibration were done in the same way as the IRTF observations using `Xtellcorgeneral` from SPEXTOOL. The FLAMINGOS spectrograph has limitations in its cooling system and this induced thermal gradients and lower S/N particularly in the *K* band, making this region unusable for analysis. Information about these observations is given in Tables 1 and 2.

2.2.2 *Archival observations*

The archival observations from the IRTF were reduced using SPEXTOOL in the same way as the targeted observations. Additional archival NIR spectra were from GNIRS at the Gemini North observatory observed with the cross-dispersed (XD) mode covering the 0.85–2.5-μm wavelength range processed using Gemini IRAF and the `XDG-NIRS` task (Mason et al. 2015). Information about the archival observations is given in Table 3.

3 SPECTROSCOPIC MEASUREMENTS

In this section, we present the spectroscopic measurements. First, we explain the emission lines' fitting method we used to measure the emission-line flux and FWHM (Section 3.1). Then, we describe absorption lines' fitting method that we apply to measure the stellar velocity dispersion (Section 3.2).

3.1 Emission lines' measurements

We fit our sample of NIR spectra in order to measure the emission-line flux and FWHM. We use `PySpecKit`, an extensive spectroscopic analysis toolkit for astronomy, which uses a Levenberg–Marquardt algorithm for fitting (Ginsburg & Mirocha 2011). We fit separately the Pa14 (0.84–0.90 μm), Pa ζ (0.90–0.96 μm), Pa δ (0.96–1.04 μm), Paγ (1.04–1.15 μm), Paβ (1.15–1.30 μm), Br10 (1.30–1.80 μm), Paα (1.80–2.00 μm) and Brγ (2.00–2.40 μm) spectral regions. An example fit is found in Fig. 2. Before applying the fitting procedure, we deredden the spectra using the galactic extinction value E_{B-V} given by the IRSA Dust Extinction Service[1] and a function from the `PySpecKit` tool.

We employ a first-order power-law fit to model the continuum. For each spectral region, we estimated the continuum level from the entire wavelength range, except where the emission lines are located (±20 Å for the narrow lines and ±150 Å for the broad

[1] http://irsa.ipac.caltech.edu/applications/DUST/docs/background.html

Table 3. Archival observations.

ID[a]	Counterpart name	Redshift	Slit size (arcsec)	Slit size (kpc)	Instrument	Type[b]	Reference
6	Mrk 335	0.0258	0.8	0.43	SpeX	1.2	Landt et al. (2008)
33	NGC 262	0.015	0.8	0.25	SpeX	1.9	Riffel et al. (2006)
116	Mrk 590	0.0264	0.8	0.44	SpeX	1.5	Landt et al. (2008)
130	Mrk 1044	0.0165	0.8	0.27	SpeX	1	Rodríguez-Ardila et al. (2002)
140	NGC 1052	0.005	0.3	0.03	GNIRS	1.9	Mason et al. (2015)
157	NGC 1144	0.0289	0.8	0.48	SpeX	2	Riffel et al. (2006)
173	NGC 1275	0.0176	0.8	0.29	SpeX	1.5	Riffel et al. (2006)
226	3C 120	0.033	0.3	0.20	GNIRS	1.5	Landt et al. (2013)
266	Ark 120	0.0323	0.8	0.53	SpeX	1	Landt et al. (2008)
269	MCG-5-13-17	0.0125	0.8	0.21	SpeX	1.5	Riffel et al. (2006)
308	NGC 2110	0.0078	0.8	0.13	SpeX	2	Riffel et al. (2006)
382	Mrk 79	0.0222	0.8	0.37	SpeX	1.5	Landt et al. (2008)
404	Mrk 1210	0.0135	0.8	0.22	SpeX	1.9	Riffel et al. (2006)
436	NGC 2655	0.0047	0.3	0.03	GNIRS	2	Mason et al. (2015)
458	Mrk 110	0.0353	0.8	0.58	SpeX	1.5	Landt et al. (2008)
477	NGC 3031	−0.0001	0.3	0.01	GNIRS	1.9	Mason et al. (2015)
484	NGC 3079	0.0037	0.3	0.02	GNIRS	2	Mason et al. (2015)
497	NGC 3227	0.0039	0.8	0.06	SpeX	1.5	Landt et al. (2008)
530	NGC 3516	0.0088	0.675	0.12	GNIRS	1.2	Landt et al. (2013)
567	H1143−192	0.0329	0.8	0.54	SpeX	1.2	Riffel et al. (2006)
579	NGC 3998	0.0035	0.3	0.02	GNIRS	1.9	Mason et al. (2015)
585	NGC 4051	0.0023	0.8	0.04	SpeX	1.5	Riffel et al. (2006)
595	NGC 4151	0.0033	0.8	0.05	SpeX	1.5	Landt et al. (2008)
607	NGC 4235	0.008	0.3	0.05	GNIRS	1.2	Mason et al. (2015)
608	Mrk 766	0.0129	0.8	0.21	SpeX	1.5	Riffel et al. (2006)
609	NGC 4258	0.001 49	0.3	0.01	GNIRS	1.9	Mason et al. (2015)
615	NGC 4388	0.0084	0.3	0.05	GNIRS	2	Mason et al. (2015)
616	NGC 4395	0.0011	0.3	0.01	GNIRS	2	Mason et al. (2015)
631	NGC 4593	0.009	0.8	0.15	SpeX	1	Landt et al. (2008)
641	NGC 4748	0.0146	0.8	0.24	SpeX	1.5	Riffel et al. (2006)
665	NGC 5033	0.0029	0.3	0.02	GNIRS	1.9	Mason et al. (2015)
697	Mrk 279	0.0304	0.8	0.50	SpeX	1.5	Riffel et al. (2006)
717	NGC 5548	0.0172	0.8	0.28	SpeX	1.5	Landt et al. (2008)
730	Mrk 684	0.0461	0.8	0.76	SpeX	1	Riffel et al. (2006)
735	Mrk 817	0.0314	0.8	0.52	SpeX	1.2	Landt et al. (2008)
739	NGC 5728	0.0093	0.8	0.15	SpeX	1.9	Riffel et al. (2006)
774	Mrk 290	0.0308	0.8	0.51	SpeX	1.5	Landt et al. (2008)
876	Arp 102B	0.0242	0.8	0.40	SpeX	1.9	Riffel et al. (2006)
994	3C 390.3	0.0561	0.675	0.78	GNIRS	1.5	Landt et al. (2013)
1090	Mrk 509	0.0344	0.8	0.57	SpeX	1.2	Landt et al. (2008)
1180	NGC 7465	0.0066	0.8	0.11	SpeX	1.9	Riffel et al. (2006)
1182	NGC 7469	0.0163	0.8	0.27	SpeX	1.5	Landt et al. (2008)
1198	NGC 7682	0.0171	0.8	0.28	SpeX	2	Riffel et al. (2013)
1287	NGC 2273	0.006 138	0.3	0.04	GNIRS	2	Mason et al. (2015)
1322	PG 0844+349	0.064	0.8	1.05	SpeX	1	Landt et al. (2008)
1348	NGC 3147	0.009 346	0.3	0.06	GNIRS	2	Mason et al. (2015)
1387	NGC 4579	0.005 06	0.3	0.03	GNIRS	2	Mason et al. (2015)

Notes. [a]*Swift*/BAT 70-month hard X-ray survey ID (http://swift.gsfc.nasa.gov/results/bs70mon/).
[b]AGN classification following Osterbrock (1981).

lines). For the modelling of the emission lines, we assume Gaussian profiles. The emission lines that we fit in each spectral region are listed in Table A1 in the appendix. The positions of the narrow lines are tied together. They are allowed to be shifted by a maximum of 8 Å (≃160 km s^{-1}) from the systemic redshift. The redshift and widths of the narrow lines are also tied together. As an initial input value for the width of the narrow lines, we used the width of the [S III]λ0.9531-μm line, which is the strongest narrow emission line in the 0.8–2.4-μm wavelength range. We set the maximum FWHM of the narrow lines to be 1200 km s^{-1}.

For the Paschen, Brackett and He Iλ1.083-μm lines, we allow the code to fit the line with a narrow component (FWHM < 1200 km s^{-1}) and a broad component (FWHM > 1200 km s^{-1}). We tied the width of the narrow component to the width of the other narrow lines present in the same spectral region. We also tied together the broad-line width of the Paschen lines that lie in the same fitting region. The broad components are allowed to be shifted by a maximum of 30 Å (≃600 km s^{-1}) from the theoretical position. This large velocity shift is motivated by the observations of a mean velocity shift of the broad Hβ to the systemic redshift of

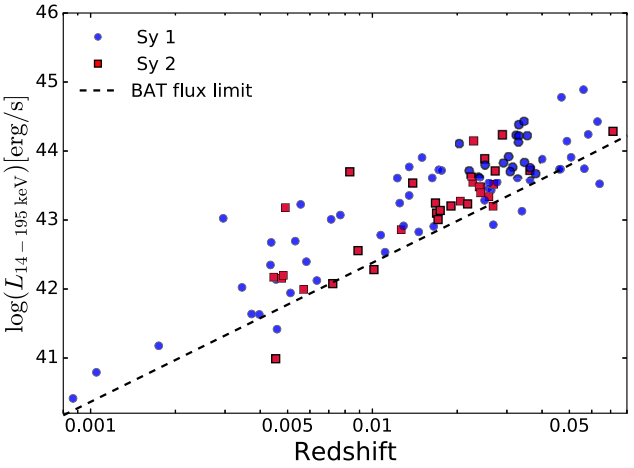

Figure 1. Distribution of the hard X-ray luminosity of the BAT AGN with respect to the redshift. The redshift is taken from NED. The dashed line shows the flux limit of the BAT 70-month survey over 90 per cent of the sky (1.34×10^{-11} erg cm^2 s^{-1}).

109 km s^{-1} with a scatter of 400 km s^{-1} in a sample of 849 quasars (Shen et al. 2016). The largest velocity shifts are ∼1000 km s^{-1}. We corrected the FWHM for the instrumental resolution, subtracting the instrumental FWHM from the observed FWHM in quadrature.

For line detection, we adopted an S/N of 3 compared to the surrounding continuum as the detection threshold. For each spectral region, we measured the noise level taking the dispersion of the continuum in a region without emission lines. In a few cases near blended regions with strong stellar absorption features (e.g. [Si VI]), a line detection seemed spurious by visual inspection even though it was above the detection limit. We have noted those with a flag and quote upper limits for these sources. If the S/N of the broad component of a particular line was below the threshold, we re-ran the fitting procedure for the spectral region of this line, without including a broad component. We inspected by eye all the spectra to verify that the broad component was not affected by residuals or other artefacts. After visual inspection, we decided to fit seven spectra with only a narrow component for Paα.

To estimate the uncertainties on the line fluxes and widths, we performed a Monte Carlo simulation. We repeated the fitting procedure 10 times, adding each time an amount of noise randomly drawn from a normal distribution with the deviation equal to the noise level. Then, we computed the median absolute deviation of the 10 measurements and we used this value as an estimate of the error at the one-sigma confidence level. We inspected visually all emission-line fits to verify proper fitting and we assigned a quality flag to each spectral fit. We follow the classification nomenclature by visual inspection of the first BASS paper (Koss et al., submitted). Quality flag 1 refers to spectra that have small residuals and very good fit. Flag 2 means that the fit is not perfect, but it is still acceptable. Flag 3 is assigned to bad fit for high S/N source due to either the presence of broad-line component or offset in emission lines. Flag 9 refers to spectra where no emission line is detected. Flag −1 means lack of spectral coverage. The emission lines' fluxes and FWHM are listed in Tables 10–19.

3.2 Galaxy templates' fitting

We used the Penalized Pixel-Fitting (PPXF) code (Cappellari & Emsellem 2004) to extract the stellar kinematics from the absorption-line spectra. This method operates in the pixel space and uses a maximum penalized likelihood approach to derive the line-of-sight velocity distributions (LOSVD) from kinematical data (Merritt 1997). First the PPXF code creates a model galaxy spectrum by convolving a template spectrum with a parametrized LOSVD. Then, it determines the best-fitting parameters of the LOSVD by minimizing the χ^2 value, which measures the agreement between the model and the observed galaxy spectrum over the set of good pixels used in the fitting process. Finally, PPXF uses the 'best-fitting spectra' to calculate σ_* from the absorption lines.

We used the same spectra as those used in Section 3.1, dereddshifted to the rest frame. Here, we concentrate on three narrow wavelength regions where strong stellar absorption features are present: CaT region (0.846–0.870 μm), CO band-heads in the *H* band (1.570–1.720 μm) and CO band-heads in the *K* band (2.250–2.400 μm). The absorption lines present in these three wavelength ranges are listed in Table A2 in the appendix. For the spectra from the FLAMINGOS spectrograph, we measured σ_* only from the CO band-heads in the *H* band, due to limited wavelength coverage.

The PPXF code uses a large set of stellar templates to fit the galaxy spectrum. We used the templates from the Miles Indo–U.S. CaT Infrared (MIUSCATIR) library of stellar spectra (Röck et al. 2015, 2016). They are based on the MIUSCAT stellar populations models, which are an extension of the models of Vazdekis et al. (2010), based on the Indo–U.S., MILES (Sánchez-Blázquez et al. 2006) and CaT (Cenarro et al. 2001) empirical stellar libraries (Vazdekis et al. 2012). The IR models are based on 180 empirical stellar spectra from the stellar IRTF library. This library contains the spectra of 210 cool stars in the IR wavelength range (Cushing, Rayner & Vacca 2005; Rayner, Cushing & Vacca 2009). The sample is composed of stars of spectral types F, G, K, M, AGB-, carbon- and S-stars, of luminosity classes I–V. Some of the stars were discarded

Table 4. Summary of instrumental set-ups.

Reference	Telescope	Instrument	N_{spectra}	Slit size (arcsec)	Grating (l per mm)	Resolving power	Wavelength range (μm)
This work	IRTF	SpeX	48	0.8	–	800	0.8–2.4
This work	KPNO	FLAMINGOS	7	1.5	–	1000	1.0–1.8
Riffel et al. (2006)	IRTF	SpeX	15	0.8	–	800	0.8–2.4
Landt et al. (2008)	IRTF	SpeX	14	0.8	–	800	0.8–2.4
Rodríguez-Ardila et al. (2002)	IRTF	SpeX	1	0.8	–	800	0.8–2.4
Riffel et al. (2013)	IRTF	SpeX	1	0.8	–	800	0.8–2.4
Mason et al. (2015)	Gemini North	GNIRS	6	0.3	31.7	1300	0.9–2.5
			7	0.3	31.7	1800	0.9–2.5
Landt et al. (2013)	Gemini North	GNIRS	2	0.675	31.7	750	0.9–2.5
			1	0.3	31.7	1800	0.9–2.5

Table 5. Relations of CLs ([Si VI] and [S VIII]) and [O III] and [S III] emission with the 14–195-keV emission and 2–10-keV emission.

Flux 1	Flux 2	Sample (1)	N (2)	σ (dex) (3)	$R_{\rm Pear}$ (4)	$p_{\rm Pear}$ (5)	p-value (6)
		Sy1	62	0.53	0.57	1.1×10^{-6}	–
[O III] λ0.5007 μm	X-ray 14–195 keV	Sy2	26	0.75	0.41	0.04	–
		All	88	0.67	0.49	1.3×10^{-6}	–
		Sy1	26	0.41	0.58	0.001	0.16
[Si VI] λ1.962 μm	X-ray 14–195 keV	Sy2	7	0.26	0.54	0.21	0.84
		All	33	0.39	0.57	0.0004	0.18
		Sy1	25	0.48	0.57	0.003	0.88
[S VIII] λ0.9915 μm	X-ray 14–195 keV	Sy2	4	0.02	0.98	0.02	(sample too small)
		All	29	0.48	0.53	0.003	0.85
		Sy1	48	0.42	0.64	1.0×10^{-6}	0.65
[S III] λ0.9531 μm	X-ray 14–195 keV	Sy2	17	0.41	0.44	0.07	0.47
		All	65	0.44	0.59	1.8×10^{-7}	0.42
		Sy1	58	0.53	0.59	1.2×10^{-6}	–
[O III] λ0.5007 μm	X-ray 2–10 keV	Sy2	25	0.57	0.65	0.0004	–
		All	83	0.64	0.58	1.1×10^{-8}	–
		Sy1	26	0.38	0.66	0.0002	0.04
[Si VI] λ1.962 μm	X-ray 2–10 keV	Sy2	6	0.36	0.11	0.83	0.01
		All	32	0.40	0.58	0.0004	0.47
		Sy1	24	0.44	0.69	0.0002	0.20
[S VIII] λ0.9915 μm	X-ray 2–10 keV	Sy2	3	0.121	0.33	0.79	(sample too small)
		All	27	0.47	0.61	0.0007	0.87
		Sy1	42	0.43	0.55	0.0001	0.85
[S III] λ0.9531 μm	X-ray 2–10 keV	Sy2	15	0.39	0.70	0.003	0.96
		All	57	0.42	0.6	1.2×10^{-6}	0.38
[O III] λ0.5007 μm	[Si VI] λ1.962 μm	All	33	0.60	0.5	0.003	
[S VIII] λ0.9915 μm	[Si VI] λ1.962 μm	All	22	0.20	0.88	9.0×10^{-8}	
[S III] λ0.9531 μm	[Si VI] λ1.962 μm	All	26	0.33	0.80	1.1×10^{-6}	

Notes. (1) AGN type; (2) size of the common sample in which Flux 1, Flux 2 and [O III] flux are available; (3) standard deviation and (4) Pearson R coefficient of the log Flux1–log Flux 2 relation; (5) Pearson p-value coefficient of the log Flux1–log Flux 2 relation; (6) p-value of the null hypothesis that this correlation coefficient and the [O III] correlation coefficient obtained from independent parent samples are equal. All coefficients are measured for the sample that has both CL emission and [O III] observations.

Table 6. Relations of CLs ([Si VI] and [S VIII]), [S III] and [O III] luminosities with the 14–195-keV emission and 2–10-keV emission.

Luminosity 1	Luminosity 2		N (1)	σ (dex) (2)	$R_{\rm Pear}$ (3)	$p_{\rm Pear}$ (4)	p-value (5)
[O III] λ0.5007 μm	X-ray 14–195 keV	All	88	0.67	0.73	8.7×10^{-16}	–
[Si VI] λ1.962 μm	X-ray 14–195 keV	All	34	0.41	0.86	5.1×10^{-11}	0.006
[S VIII] λ0.9915 μm	X-ray 14–195 keV	All	29	0.49	0.83	2.9×10^{-8}	0.916
[S III] λ0.9531 μm	X-ray 14–195 keV	All	65	0.48	0.83	2.5×10^{-17}	0.002
[O III] λ0.5007 μm	X-ray 2–10 keV	All	83	0.64	0.75	1.9×10^{-16}	–
[Si VI] λ1.962 μm	X-ray 2–10 keV	All	32	0.41	0.87	1.6×10^{-10}	0.019
[S VIII] λ0.9915 μm	X-ray 2–10 keV	All	27	0.46	0.86	1.1×10^{-8}	0.744
[S III] λ0.9531 μm	X-ray 2–10 keV	All	57	0.49	0.84	2.1×10^{-16}	0.002

Notes. (1) Size of the common sample in which both Luminosity 1 and Luminosity 2 are available; (2) standard deviation and (3) Pearson R coefficient of the log Flux1–log Flux 2 relation; (4) Pearson p-value coefficient of the log Flux1–log Flux 2 relation; (5) p-value of the null hypothesis that this correlation coefficient and the [O III] correlation coefficient obtained from independent parent samples are equal.

because of their unexpected strong variability, strong emission lines or not constant baseline. The IR models cover the spectral range 0.815–5.000 μm at a resolving power $R = 2000$, which corresponds to a spectral resolution of FWHM $\sim$ 150 km s^{-1} ($\sigma \sim$ 60 km s^{-1}) equivalent to 10 Å at 2.5 μm (Röck et al. 2015). A comparison with Gemini Near-Infrared Late-type stellar (GNIRS) library (Winge, Riffel & Storchi-Bergmann 2009) in the range 2.15–2.42 μm at $R = 5300$–5900 (resolution of ∼3.2 Å FWHM) is provided in the appendix. The spectral templates are convolved to the instrumental resolution of the observed spectra under the assumption that the shapes of the instrumental spectral profiles are well approximated by Gaussians.

Table 7. Relations of CLs and [S III] luminosity with the 14–195-keV emission and 2–10-keV emission.

Line	2–10 keV					14–195 keV			
	N_{undet}	N_{det}	X-ray-to-line ratio	Slope	Intercept	N_{det}	X-ray-to-line ratio	Slope	Intercept
	(1)	(2)	(3)	(4)	(5)	(6)	(7)	(8)	(9)
[S III] λ0.9531 μm	6	57	227	1.20 ± 0.11	−11.30 ± 4.78	65	587	1.11 ± 0.10	−7.81 ± 4.43
[Ca VIII] λ2.3210 μm	76	8	7913	1.00 ± 0.53	−4.04 ± 22.7	8	16448	−0.67 ± 0.37	67.74 ± 16.01
[Si VI] λ1.962 μm	42	32	1247	1.02 ± 0.13	−4.02 ± 5.92	34	3217	0.83 ± 0.13	−0.75 ± 5.75
[S VIII] λ0.9915 μm	62	27	2756	1.18 ± 0.15	−11.31 ± 6.52	29	5472	1.00 ± 0.15	−4.03 ± 6.35
[S IX] λ1.2520 μm	76	18	4177	1.00 ± 0.22	−3.92 ± 9.45	18	9239	0.91 ± 0.17	−0.16 ± 7.53
[Fe XIII] λ1.0747 μm	84	4	3754	0.44 ± 0.70	20.43 ± 30.08	4	8886	0.54 ± 1.01	15.6 ± 43.37
[Si X] λ1.4300 μm	79	17	3481	0.96 ± 0.17	−1.77 ± 7.42	18	8877	1.02 ± 0.23	−5.14 ± 9.9

Notes. (1) Number of sources with no line detection in clean atmospheric regions for which the upper limits are measured; (2) size of the sample in which both line luminosity and 2–10-keV intrinsic X-ray luminosity are measured; (3) mean 2–10-keV X-ray-luminosity-to-line-luminosity ratio for the sources with line detection (upper limits are not considered); (4) slope a and (5) intercept b of the ordinary least squares (OLS) bisector fit $\log L_{\rm Line} = a \times \log L_{2-10\,\rm keV} + b$ for the sources with line detection; (6) size of the sample in which both line luminosity and 14–195-keV X-ray luminosity are available; (7) mean 14–195-keV X-ray-luminosity-to-line-luminosity ratio for the sources with line detection (upper limits are not considered); (8) slope a and (9) intercept b of the OLS bisector fit $\log L_{\rm Line} = a \times \log L_{14-195\,\rm keV} + b$ for the sources with line detection.

We applied a mask when fitting stellar templates around the following emission lines: Pa14 (in the CaT region), [Fe II]λ16436, [Fe II]λ16773 and Br11 λ16811 (in the *H* band), and [Ca VIII]λ23210 (in the *K* band). Since the [Ca VIII]λ23210 emission line overlaps with the CO(3–1) λ23226 absorption line, we decided to mask the region around this line only if the emission line was detected. Also for the Pa14 line, we decided to mask the line only if the emission line was detected, because it is in the same position of the Ca IIλ8498 absorption line and therefore it is in a critical region for the measurement of the velocity dispersion. We set the width of the emission lines' mask to 1600 km s^{-1} for the narrow lines and to 2000 km s^{-1} for the Brackett and Paschen lines (Br11 and Pa14). The error on the velocity dispersion ($\Delta\,\sigma_*$) is the formal error (1σ) given by the PPXF code. The error is in the range 1–20 per cent of the σ_*values.

All absorption lines' fits were inspected by eye to verify proper fitting. We follow the nomenclature of fitting classification of the first BASS paper (Koss et al., submitted). We assigned the quality flag 1 to the spectra that have small residuals and very good fit of the absorption lines (average error $\langle\Delta\sigma_*\rangle = 6$ km s^{-1}). Quality flag 2 refers to the spectra that have larger residuals and errors in the velocity dispersion value (average error $\langle\Delta\sigma_*\rangle = 12$ km s^{-1}), but the absorption lines are well described by the fit. For spectra where the error of the velocity dispersion value is >50 km s^{-1} and the fit is not good, we assigned the flag 9.

4 RESULTS

We first compare the FWHM of broad Balmer and Paschen lines (Section 4.1). Then, we discuss AGN that show 'hidden' broad lines in the NIR spectrum but not in the optical (Section 4.2). Next, we measure the velocity dispersion (Section 4.3) and black hole masses (Section 4.4). In Section 4.5, we apply NIR emission-line diagnostics to our sample. Then, we discuss the presence of CLs in the AGN spectra (Section 4.6). Finally, we measure the correlation between CL and hard X-ray emission (Section 4.7).

4.1 Comparison of the line widths of the broad Balmer and Paschen lines

We compared the line widths of the broad components of Paβ, Paα, Hβ and Hα. Fig. 3 shows the comparison between the FWHM of the broad Paβ and Hβ with or without fitting Fe templates to the Hβ region (e.g. Boroson & Green 1992; Trakhtenbrot & Netzer 2012). We fitted the data using a linear relation with fixed slope of 1 and we searched for the best intercept value. We equally weight each data point in the line fit because the measured uncertainties from statistical noise are small (<5 per cent). For the FWHM of the broad Paβ and Hβ with Fe fitting, we found the best fit to have an offset of 0.029 ± 0.003 dex with a scatter of $\sigma = 0.08$ dex. Without Fe fitting, we find a linear relation with an offset of −0.019 ± 0.005 dex and a larger scatter ($\sigma = 0.13$ dex). After taking into account the effect of the iron contamination on Hβ, we did not find a significant difference between the FWHM of Hβ and the FWHM of Paβ (the p-value of the Kolmogorov–Smirnov test is 0.84). For the FHWM of Paβ to Hα, we find an offset of −0.023 ± 0.03 dex and a scatter $\sigma = 0.1$ dex with no significant difference between their distributions (Kolmogorov–Smirnov test p-value = 0.56).

We observed a trend for the mean FWHM of Paα to be smaller than the FWHM of the other lines. Comparing the FWHM of Paα and Hβ we found the best fit to have an offset of 0.092 ± 0.005 dex with a scatter $\sigma = 0.09$ dex, while for the comparison between Paα and Hα, the offset is 0.094 ± 0.006 dex with a scatter $\sigma = 0.13$ dex. For the comparison between Paα and Paβ, the offset is 0.093 ± 0.005 dex, with a scatter $\sigma = 0.08$ dex. Considering the mean values, we found that that the mean value of the FWHM of Paα (2710 ± 294 km s^{-1}) is smaller than the mean value of Hα and Hβ (3495 ± 436 and 3487 ± 582 km s^{-1}, respectively). For the sources with measurements of the broad components of both Paα and Paβ, the mean value of the FWHM of Paα (2309 ± 250 km s^{-1}) is also smaller than the mean value of Paβ (2841 ± 283 km s^{-1}). We note that none of these differences rises to the 3σ level, so a larger sample would be required to study whether the FWHM of broad Paα is indeed smaller than the other lines.

We used the Anderson–Darling and Kolmogorov–Smirnov to further test if the distribution of the FWHM of Paα is significantly different from those of the other lines. We find that both tests indicate that the populations are consistent with being drawn from the same intrinsic distribution at the greater than 20 per cent level for all broad lines. For the comparison of Paα with Hβ, the Kolmogorov–Smirnov test gives a p-value = 0.67, whereas for the comparison of Paα with Hα the p-value is 0.33 and for Paα with Paβ the p-value is 0.63 suggesting no significant difference in the distributions of the FWHM of the broad components.

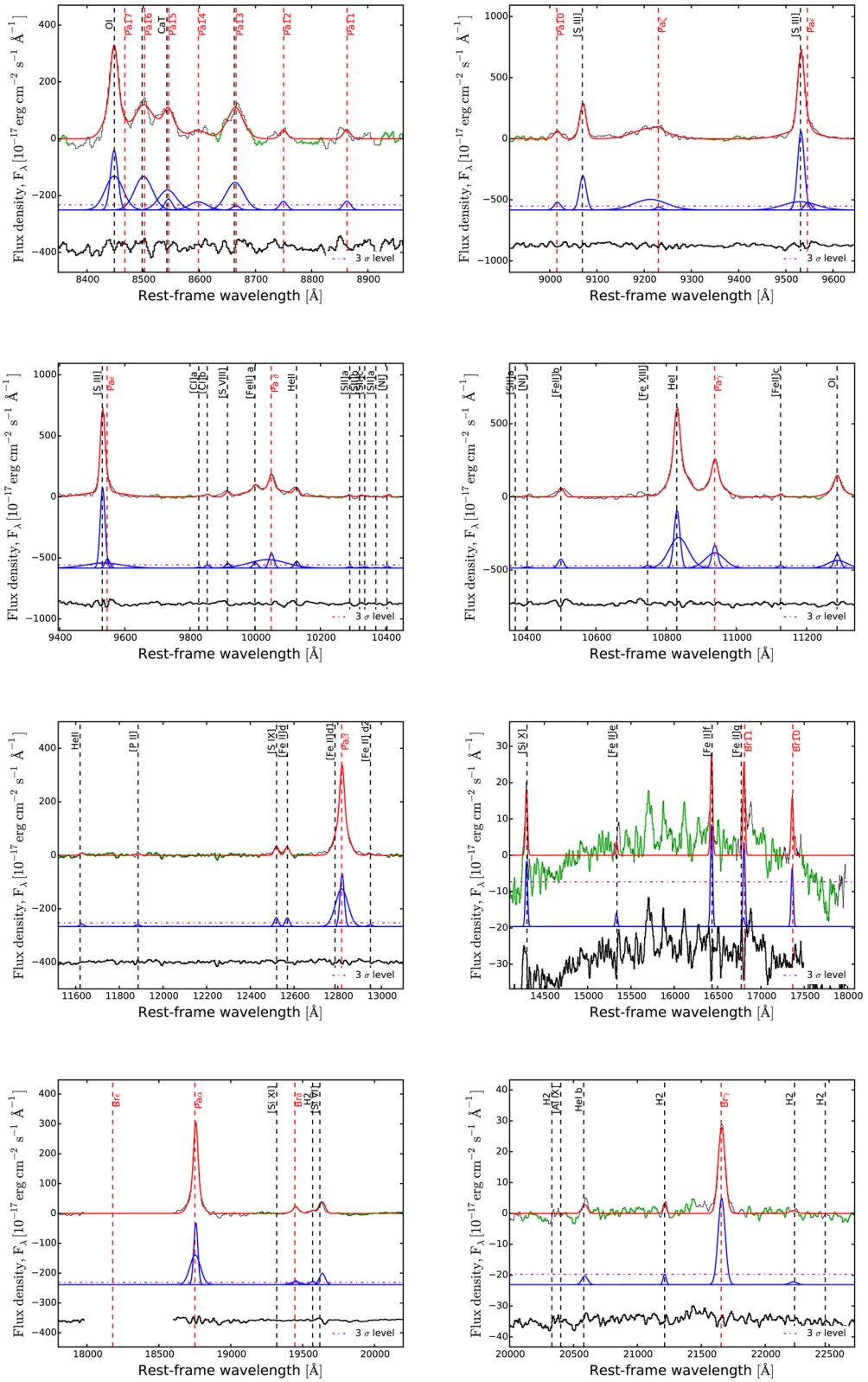

Figure 2. Example of emission lines' fits for galaxy 2MASX J19373299−0613046 for which the spectrum was taken with IRTF. The eight panels show the emission lines' fits for the regions (from the upper left to the bottom right): Pa14, Pa ζ, Pa δ, Paγ, Paβ, Br10, Paα and Brγ. In the upper part of each figure, the spectrum is shown in black and the best fit in red. The regions where the continuum is measured are shown in green. In the middle part of the figure, the components of the fit are shown in blue and the magenta dashed line shows the threshold level for detection (S/N > 3). The lower part of the figure shows the residuals in black.

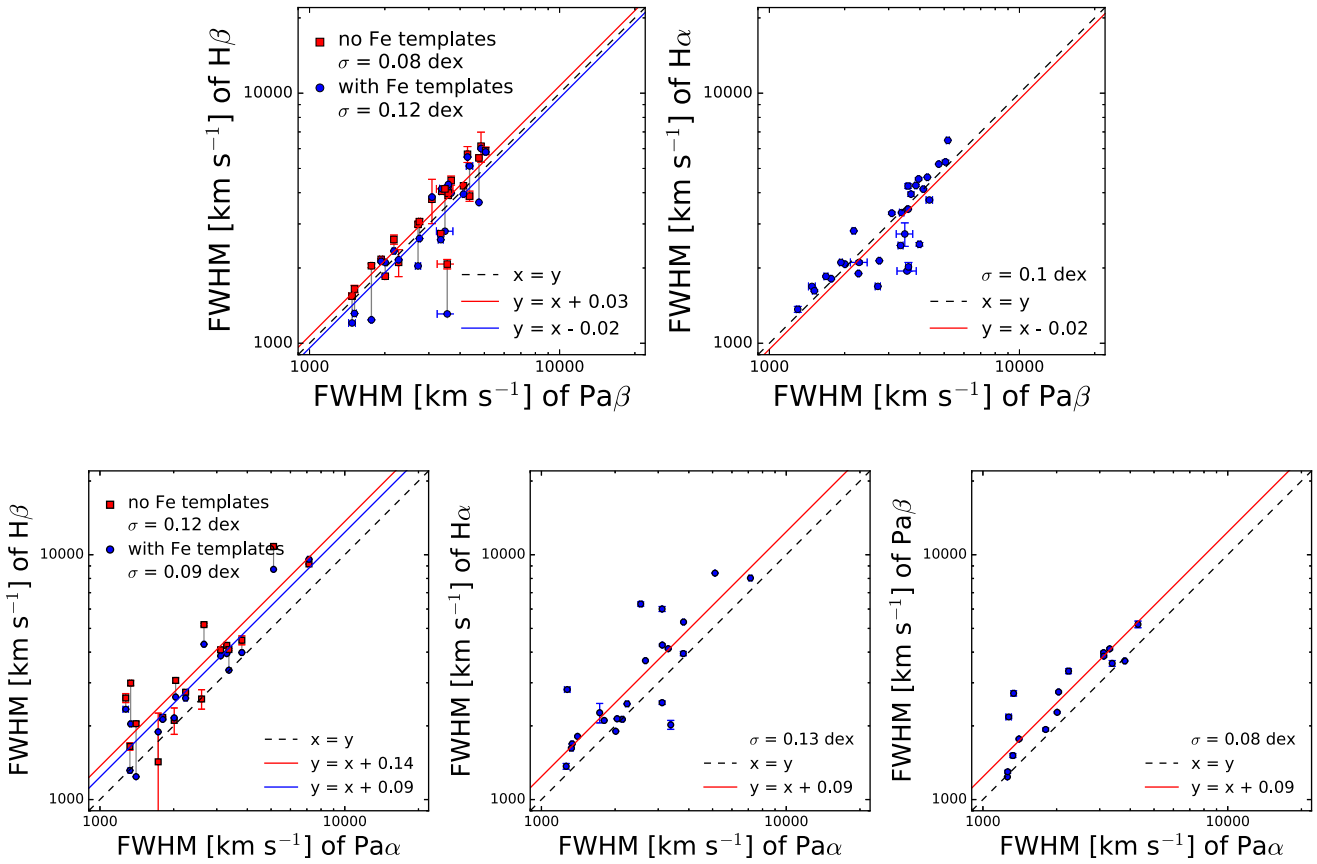

Figure 3. Upper panels: comparison between the FWHM of the broad components Paβ and Hβ (left). The red points show the FWHM of Hβ measured without taking into account the iron contamination and the instrumental resolution and the blue points the FWHM of Hβ measured using iron templates and corrected for the instrumental resolution. The black dashed line shows the one-to-one relation, the red and blue lines show the linear fit with slope 1. The right-hand panel shows the comparison between the FWHM of the broad component of Paβ and Hα. Lower panels: comparison of the FWHM of the broad components of Paα with Hβ (left), Hα (middle) and Paβ (right).

4.2 Hidden BLR

In our sample, there are 33 AGN classified as Seyfert 2 based on the lack of broad Balmer lines in the optical spectral regime. We found three of these (9 per cent) to show broad components (FWHM $>$ 1200 km s^{-1}) in either Paα and/or Paβ. An example is shown in Fig. 4. For Mrk 520 and NGC 5252, we detected the broad component of both Paα and Paβ and also of He I 1.083 µm. For NGC 5231, we detected broad Paα, but the broad Paβ component is undetected. For all three galaxies, we did not observe a broad component in the other Paschen lines. We do not detect a broad component in the Paschen lines for 16/33 (49 per cent) Seyfert 2 galaxies, in agreement with their optical measurements. For the remaining 14/33 (42 per cent) sources, we could not detect the broad components because the line is in a region with significant sky features.

We considered the values of $N_{\rm H}$ measured by Ricci et al. (2015) and Ricci et al. (submitted). The Seyfert 2s in our sample have column densities in the range $\log N_{\rm H}$ = 21.3–25.1 cm^{-2} with a median of $\log N_{\rm H} = 23.3$ cm^{-2}. The three AGN showing a 'hidden' BLR in the NIR belong to the bottom 11 percentile in $\log N_{\rm H}$ (Fig. 5) among the Seyfert 2s in our sample ($\log N_{\rm H} < 22.4$ cm^{-2}).

Next, we considered the optically identified Seyfert 1 in our sample, and we investigated the presence of broad lines in their NIR spectra. In the Seyfert 1–1.5 in our sample, we did not find spectra that lack the broad Paα or Paβ component.

For the optical Seyfert 1.9 in our sample, the NIR spectra in general show broad lines except for some objects with weak optical broad lines. We found broad Paschen lines in 10/23 (44 per cent) Seyfert 1.9. For 6/23 (26 per cent) of Seyfert 1.9, the spectra do not cover the Paα and Paβ regions. There are 7/23 Seyfert 1.9 (30 per cent) that do not show broad components in Paα and Paβ. All these galaxies have $\log N_{\rm H} > 21.5$ cm^{-2}. Four of them have a weak broad component of Hα compared to the continuum (EQW[b Hα] $<$ 36 Å). Further higher sensitivity studies are needed to test whether the broad Hα component is real or is a feature such as a blue wing.

4.3 Velocity dispersion

We measured the stellar velocity dispersion (σ_*) from the CaT region and from the CO band-heads in the *H* band and in the *K* band. The results are tabulated in Table 8. Examples of σ_* fitting are available in Appendix A2. In total, we could measure σ_* only for 10 per cent (10/102) of objects using the CaT region. The main reasons for this are as follows: lack of wavelength coverage of the CaT region, absorption lines too weak to be detected and presence of strong Paschen emission lines (Pa10 to Pa16) in the same wavelength of the CaT. We have a good measurement of σ_* for 31/102 (30 per cent) objects from the CO band-heads in the *K* band and for 54/102 (53 per cent) from the CO band-heads in the *H* band. We found that σ_* measured from the CaT region and from the CO band-heads (*H*

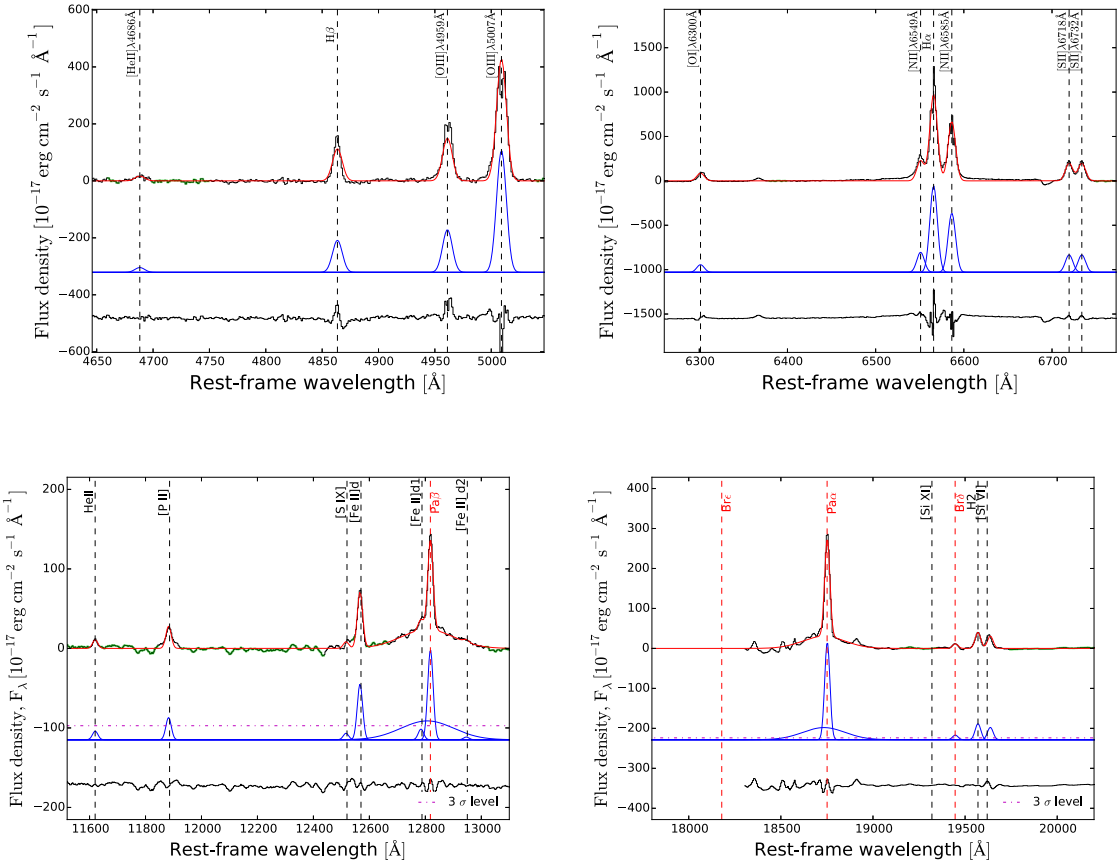

Figure 4. Optical and NIR spectra of Mrk 520, which is an example of Seyfert 2 galaxy displaying a 'hidden' BLR in the NIR. Upper panels: optical spectrum of the Hβ and Hα region. The best fit is in red, the model in blue and the residuals in black. Lower panels: NIR spectrum of the Paβ and Paα region. In addition to the components explained above, the magenta dashed line in the middle part of the figures shows the detection threshold (S/N > 3) with respect to the fitting continuum (blue).

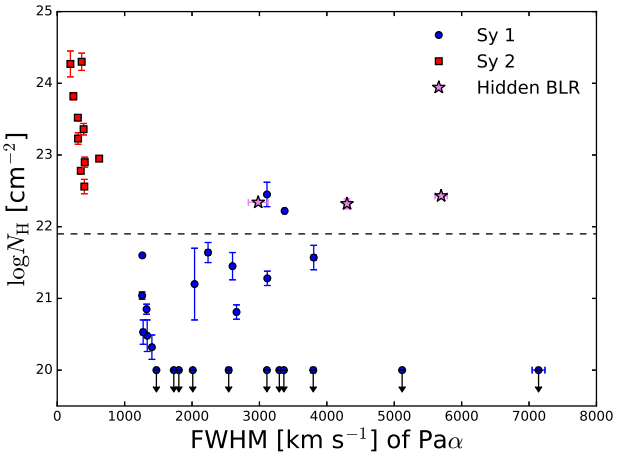

Figure 5. Distribution of column density $N_{\rm H}$ as a function of the FWHM of Paα. Blue points are Seyfert 1 which show a BLR in Hα, red squares are Seyfert 2 and violet stars are the Seyfert 2 with narrow lines in Hα that show a hidden BLR in the Paα. The dashed line shows the threshold $N_{\rm H}$ value that separates optical Seyfert 1 and Seyfert 2 using the Hβ line (Koss et al., submitted).

and *K* bands) are in good agreement (median difference 0.03 dex). However, we compared these measurements with literature values of σ_* measured in the optical and we found that the σ_* measured from the NIR absorption lines are ∼30 km s^{-1} larger, on average, than the σ_* measured in the optical range (median difference 0.09 dex). Further details about the comparison of σ_* measured in the different NIR spectral regions and in the optical is provided in Appendix A2.

4.4 Black hole masses

We derived the black holes masses from the velocity dispersion and from the broad Paschen lines. For the cases where we have both $\sigma_{*,\rm CO}$ and $\sigma_{*,\rm CaT}$, we use $\sigma_{*,\rm CO}$, since this method could be used for more sources with higher accuracy. We used the following relation from Kormendy & Ho (2013) to estimate the $M_{\rm BH}$ from σ_*:

$$\log\left(\frac{M_{\rm BH}}{\rm M_\odot}\right) = 4.38 \times \log\left(\frac{\sigma_*}{200\,\rm km\,s^{-1}}\right) + 8.49\ . \quad (1)$$

This relation has an intrinsic scatter on log $M_{\rm BH}$ of 0.29 ± 0.03. There are different studies that derived prescriptions to estimate $M_{\rm BH}$ from the broad Paschen lines (Paα or Paβ). All these methods use the FWHM of the Paschen lines Paα or Paβ. Since Paα is near a region of atmospheric absorption, we have more measurements of the broad component of Paβ; therefore, we prefer to use this line to derive $M_{\rm BH}$. As an estimator of the radius of the BLR, previous studies used the luminosity of the 1-μm continuum (Landt et al. 2011a), the luminosity of broad Paα or Paβ (Kim et al. 2010, La Franca et al. 2015) or the hard X-ray luminosity (La Franca et al. 2015). We use the luminosity of broad Paβ, since the continuum luminosity at

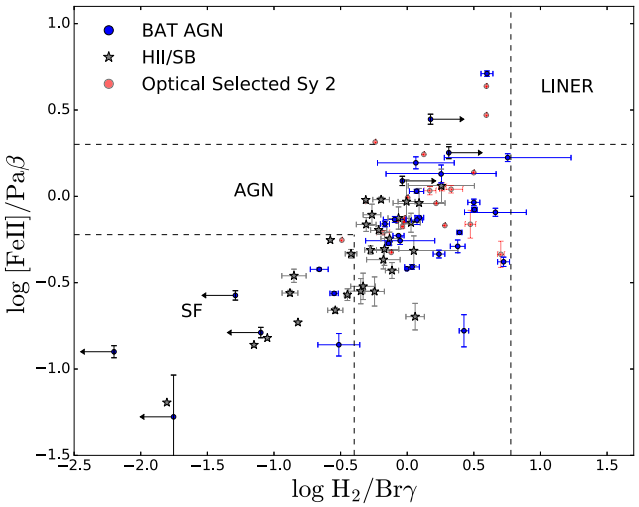

Figure 6. NIR emission lines' diagnostic diagram from Riffel et al. (2013). In blue are the AGN of our sample. In grey are shown the sample of starburst galaxies (SBGs) from Riffel et al. (2006); the sample of SBGs and H II region from Larkin et al. (1998), Dale et al. (2004) and Martins et al. (2013). In red are shown the sample of Seyfert 2 from Riffel et al. (2006) and Veilleux et al. (1997).

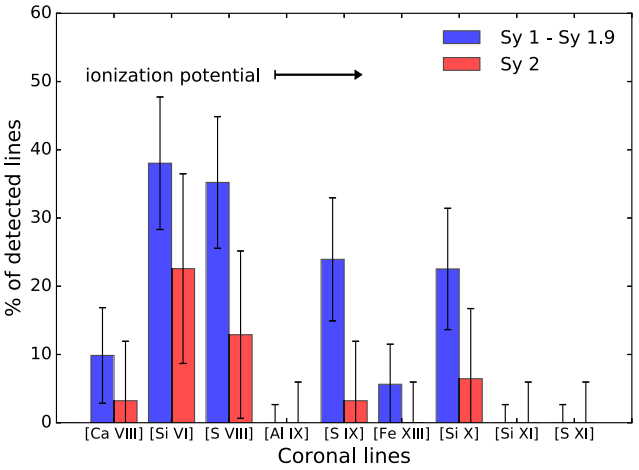

Figure 7. Percentage of CL detections in Seyfert 1 and Seyfert 2. The CLs are ordered by increasing ionization potential (IP) from left to right ([Ca VIII]: 127.7 eV, [Si VI]: 166.8 eV, [S VIII]: 280.9 eV, [Al IX]: 284.6 eV, [S IX]: 328.2 eV, [Fe XIII]: 330.8 eV, [Si X]: 351.1 eV, [Si XI]: 401.4 eV, [S XI]: 447.1 eV).

1 μm can be contaminated by emission from stars and hot dust and the hard X-ray luminosity is not observed simultaneously with the Paschen lines. We use the following formula from La Franca et al. (2015) that was calibrated against reverberation-measured masses assuming a virial factor $f = 4.31$:

$$\frac{M_{\rm BH}}{\rm M_\odot} = 10^{7.83\pm0.03}\left(\frac{L_{{\rm Pa}\beta}}{10^{40}\ {\rm erg\ s^{-1}}}\right)^{0.436\pm0.02} \times \left(\frac{{\rm FWHM_{Pa}}\beta}{10^{4}\ {\rm km\ s^{-1}}}\right)^{1.74\pm0.08}. \quad (2)$$

This relation has an intrinsic scatter on log $M_{\rm BH}$ of 0.27. The values of $M_{\rm BH}$ are listed in Table 9. For 46/102 (45 per cent) AGN, we have the $M_{\rm BH}$ from $\sigma_{*,\rm CO}$ and for 34/102 (33 per cent) we have the $M_{\rm BH}$ from Paβ. Considering the cases where we have both measurements, we have $M_{\rm BH}$ measurements for 69/102 (68 per cent) AGN in our sample. Using 11 objects that have both $\sigma_{*,\rm CO}$ and Paβ measurements of $M_{\rm BH}$, we found that $M_{\rm BH}$ derived from $\sigma_{*,\rm CO}$ are larger than $M_{\rm BH}$ derived from broad lines by up to 1 dex. A detailed discussion of the results using different black hole mass estimators and comparison to mass measurements in the optical is provided in the Appendix A3.

4.5 NIR emission-line diagnostic diagram

NIR emission-line diagnostics (e.g. Riffel et al. 2013) use combinations of NIR lines ([Fe II] 1.257 μm and Paβ in the J band, H_2 2.12 μm and Brγ in the K band) to identify AGN. We detected the four lines needed for the diagnostic in 25 per cent (25/102) of AGN (Fig. 6). Most of these objects (88 per cent, 22/25) are identified as AGN in the NIR diagnostic diagram, whereas three objects lie in the SF region.

Moreover, SFGs from past studies (Larkin et al. 1998; Dale et al. 2004; Martins et al. 2013) overlap with AGN in the diagram. Considering the AGN in our sample, and SFGs and AGN line ratios from the literature, the fraction of SFGs in the AGN region is 20/30 (67 ± 13 per cent), whereas the fraction of AGN in the AGN region is 45/53 (85 ± 7 per cent).

For the AGN where we do not detect either H_2 or Brγ, we used upper limits. All the three AGN that have upper limits on Brγ are in the AGN region of the diagram, although if we consider the upper limit, they could also be in the low-ionization nuclear emission-line region galaxies (LINER). All the four objects with no detection of H_2 are in the star-forming region. We found that all the nine Seyfert 2 galaxies where emission lines were detected are selected as AGN, whereas the objects in the SF region are broad-line objects.

The result of the Kolmogorov–Smirnov test is that the distributions of [Fe II]/Paβ for AGN and SFGs are consistent with being drawn from the same distribution (p-value = 0.063), whereas distribution of H2/Brγ are significantly different (p-value = 0.000 24). Thus the SF line ratios [Fe II]/Paβ are indistinguishable from AGN.

4.6 Coronal lines

In this section, we report the number of CL detections in our sample. Table A4 in the appendix provides a list of the fitted lines. Fig. 7 shows the percentage of spectra in which we detected each CL, divided by Seyfert 1 and Seyfert 2.

We observe a trend for the number of CL detections to increase with decreasing IP. We found that the CL with the highest number of detections is [Si VI] (34 detections, 33 per cent), followed by [S VIII] (29 detections, 28 per cent). The [Ca VIII] line does not follow this trend, since it is detected only in eight objects (8 per cent). This line has the lowest IP (127.7 eV) among the CLs. There are three CLs ([Al IX], [Si XI] and [S XI]) that are not detected in any AGN spectra. [Si XI] and [S XI] have the highest IPs among the CLs, while [Al IX] has an intermediate value.

We detect at least one CL in 44/102 (43 per cent) spectra in our sample, but only 18/102 (18 per cent) have more than two CLs detected. Considering Seyfert 1 and Seyfert 2 separately, the percentage of objects with at least one CL detection is higher in Seyfert 1 (53 ± 10 per cent) than in Seyfert 2 (20 ± 10 per cent).

4.7 Coronal lines and X-ray emission

In order to test whether the strength of CL emission is stronger in Seyfert 1 than in Seyfert 2 for the same intrinsic AGN bolometric luminosity measured from the X-rays, we applied a survival analysis to take into account the fact that our data contains a number of upper limits [41 per cent (42/102)] as well as emission-line regions that were excluded because of atmospheric absorption [12 per cent (12/102)]. We used the ASURV package (Feigelson & Nelson 1985), which applies the principles of survival analysis. Specifically, we measure the ratio of [Si VI] emission divided by the 14–195-keV X-ray emission, which is a proxy for the AGN bolometric luminosity (e.g. Vasudevan & Fabian 2009). We then compare the distributions of ratios for Seyfert 1 and Seyfert 2 using the ASURV Two Sample tests. We find that the ratio of CL emission to X-ray emission in Sy 1 is significantly different than in Sy 2 at the less than 1 per cent level, in the various survival analysis measures (e.g. Gehan's Generalized Wilcoxon Test, Logrank Test, etc.). This means that for the same X-ray luminosity, CL emission is stronger in Sy 1 than in Sy 2, consistent with the higher detection fraction of CL in Sy 1.

We study the correlation between the CL and the hard X-ray continuum (14–195 keV) emission (Fig. 8 and 9). We focus on the [Si VI] 1.962-μm emission line (IP = 166.8 eV), because it is the CL that is detected in the largest number of spectra. We fit the data using the ordinary least squares (OLS) bisector fit method as recommended when there are uncertainties in both the X and Y data (Isobe et al. 1990). The OLS fitting method takes into account the uncertainties in both fluxes. The relation between the [Si VI] and the X-ray emission (14–195 keV) shows a scatter of $\sigma = 0.39$ dex and a Pearson correlation coefficient $R_{\rm pear} = 0.57$ ($p_{\rm Pear} = 0.0005$). The relation between the [O III] flux and the X-ray flux shows a scatter of $\sigma = 0.53$ dex and a Pearson correlation coefficient $R_{\rm pear} = 0.45$ ($p_{\rm Pear} = 0.009$). We ran a Fischer Z-test to investigate whether the intrinsic scatter in the correlation between [Si VI] and X-ray emission is significantly better than the one between [O III] and X-ray emission and found a p-value = 0.18, suggesting the two correlations are not significantly different. Using the 2–10-keV intrinsic emission, the correlation with [Si VI] is similar as at 14–195 keV ($\sigma = 0.40$, $R_{\rm Pear} = 0.58$, $p_{\rm Pear} = 0.0004$). We note that the uncertainties on the 2–10-keV flux are not provided, but are dominated by the difficulties in measuring the column density. Therefore, for the fit we took into account only the uncertainties on the line fluxes.

We compared also the flux of [Si VI] and [O III]. We found a scatter of $\sigma = 0.60$ that is slightly larger than the scatter in the [Si VI] versus hard X-ray ($\sigma = 0.51$). The correlation coefficient is $R_{\rm Pear} = 0.50$ ($p_{\rm Pear} = 0.003$). We ran the Z-test and we found p-value = 0.76. Thus, [Si VI] correlates with [O III] almost at the same level as with the hard X-ray. We found that the correlation between CLs is stronger than the one between [Si VI] and [O III]. For example, the correlation of [Si VI] with [S VIII] has a correlation coefficient $R_{\rm Pear} = 0.88$ ($p_{\rm Pear} = 2.1 \times 10^{-7}$), which is significantly stronger than the one with [O III] (Z-test p-value $= 8.3 \times 10^{-5}$).

We also test the correlations in Seyfert 1 and Seyfert 2 separately. For the six Seyfert 2 with good flux measurements of [Si VI] and [O III], the relation between the [Si VI] flux and the BAT X-ray flux shows a scatter of $\sigma = 0.27$ dex and a Pearson correlation coefficient $R_{\rm Pear} = 0.59$ ($p_{\rm Pear} = 0.22$), whereas the relation between the [O III] and X-ray emission shows a scatter of $\sigma = 0.65$ dex and a Pearson correlation coefficient $R_{\rm Pear} = 0.53$ ($p_{\rm Pear} = 0.27$). A Fischer Z-test gives a p-value = 0.84, meaning that the two correlations are not significantly different. We have 27 Seyfert 1 galaxies with good flux measurements of [Si VI] and [O III]. For these sources, we found the Pearson correlation coefficient $R_{\rm Pear} = 0.58$ ($p_{\rm Pear} = 0.001$) in the comparison between [Si VI] and hard X-ray and $R_{\rm Pear} = 0.43$ ($p_{\rm Pear} = 0.02$) in the comparison between [O III] and hard X-ray. We ran the Z-test and we found a p-value = 0.16, meaning that the two correlations are not significantly different.

Next, we considered the correlation between [O III], [Si VI] and hard X-ray luminosity (14–195 keV). The correlation coefficient of X-ray luminosity with the [Si VI] luminosity ($R_{\rm Pear} = 0.86$) is higher than the correlation coefficient with the [O III] luminosity ($R_{\rm Pear} = 0.74$). The Fischer Z-test gives a p-value = 0.006, meaning that the two correlations are significantly different. This suggests that the CL luminosity does show a significantly reduced scatter than the [O III] luminosity when compared to the X-ray emission.

We considered also [S III]λ 0.9531 μm, which is an NIR emission line with lower IP (= 23.3 eV). The correlation of the hard X-ray with [Si VI] luminosity ($R_{\rm Pear} = 0.87$) is similar to the correlation with [S III] luminosity ($R_{\rm Pear} = 0.85$). For the 26 sources that have both the [Si VI] and [S III] line detections, the Fischer Z-test gives a p-value = 0.5, meaning that the two correlations are not significantly different.

For the 24 sources that also have 2–10-keV luminosity measurement, the correlation of the 2–10-keV luminosity with [Si VI] ($R_{\rm Pear} = 0.90$, $\sigma = 0.39$ dex) is stronger than the correlation with [S III] luminosity ($R_{\rm Pear} = 0.84$, $\sigma = 0.52$ dex). However, the Fischer Z-test gives a p-value = 0.08, suggesting that the [Si VI] luminosity does not have a significantly reduced scatter than the [S III] luminosity when compared to the X-ray emission.

5 DISCUSSION

5.1 Comparison of the FWHM of the broad Balmer and Paschen lines

Landt et al. (2008) observed a trend for the FWHM of Hβ to be larger than the FWHM of Paβ. They claimed that it might be due to the effect of the Hβ 'red shelf', caused by the emission from the Fe II multiplets. This emission on the red side of Hβ can contaminate the broad component of Hβ, so that the measured FWHM appear broader. We compared the FWHM of Paβ with the FWHM of Hβ, measured taking into account the emission from the Fe II multiplets and we found that the FWHM of Hβ is not systematically different from the FWHM of Paβ, suggesting that these two lines are produced in the same region. Using a larger sample of broad-line sources ($N = 22$), we do not find a statistically significant difference in the intrinsic distributions of the FWHM of Paα with respect to the other broad lines, as Landt et al. (2008) found with a smaller number of broad-line AGN ($N = 18$). We note that the estimates of line FWHM performed in Landt et al. (2008) were done using a different method, where the narrow lines were subtracted before fitting broad lines as opposed to the simultaneous fit in this study.

A similar result is presented in a recent paper by Ricci et al. (2016). They analysed a sample of 39 AGN, and found a good correlation of the FWHM of the broad Hα, Hβ, Paα, Paβ and He I λ1.083-μm lines, with small offsets. They found less scatter around the relation, and this can be due to the fact that they have more 'quasi-simultaneous' observations.

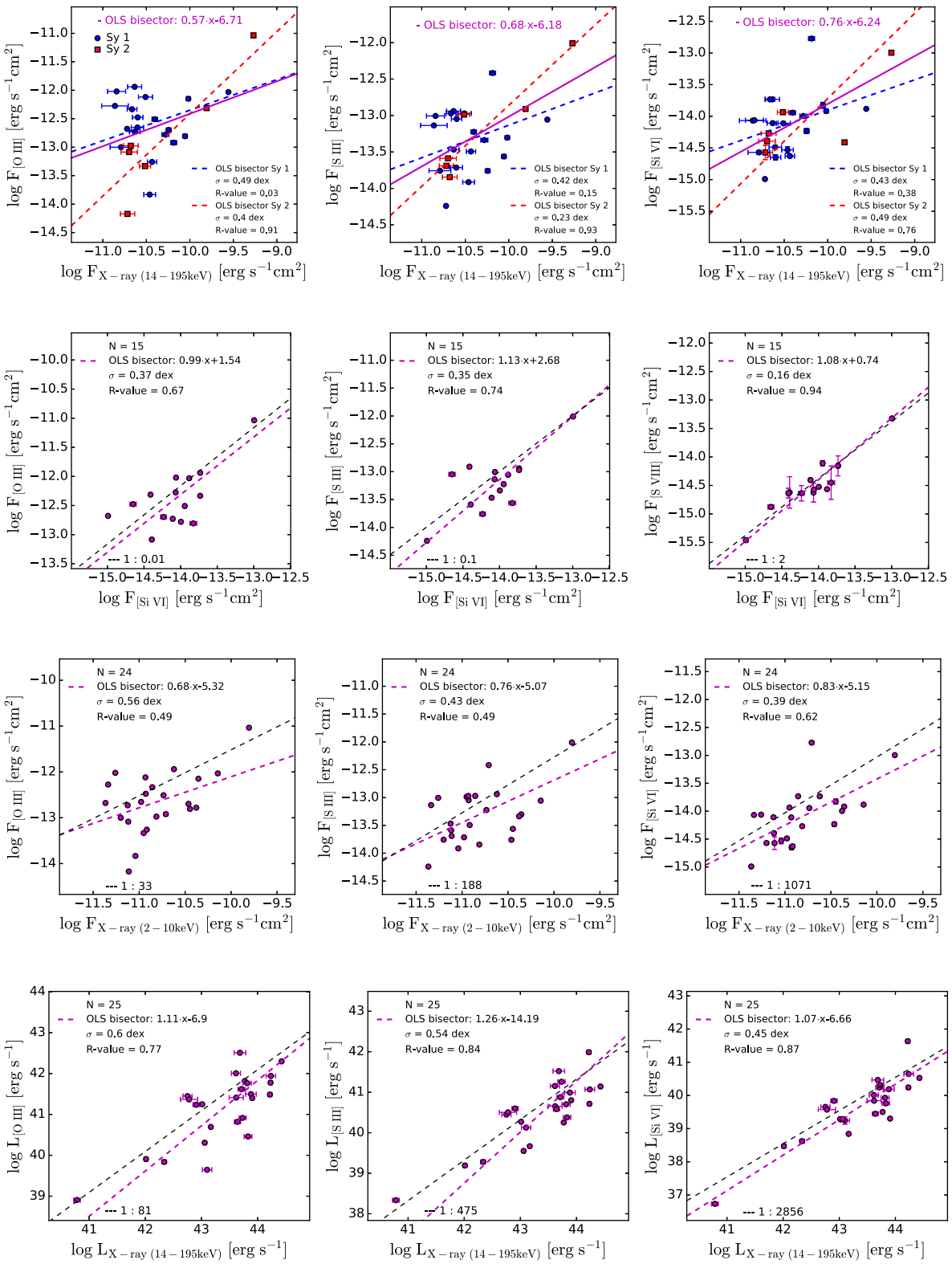

Figure 8. Plots comparing the scatter for a sample of AGN with line detections in each line to compare the overall scatter. Blue points are Seyfert 1 and red squares are Seyfert 2. The black dashed lines have slope 1 and are scaled according to the mean flux ratio. The magenta line is the ordinary least squares (OLS) bisector fit for the entire sample. Upper panels: relation of the hard X-ray emission (14–195 keV) with [O III] (left), [S III] λ0.9531 μm (middle) and [Si VI] (right). Second-row panels: relation of the [Si VI] flux with [O III] (left), [S III] (middle) and [S VIII] (right) for the same sample of AGN. Third-row panels: relation of the hard X-ray flux (2–10 keV) with [O III] (left), [S III] (middle) and [Si VI] (right) for the same sample of AGN. Bottom-row panels: relation of the hard X-ray luminosity (14–195 keV) with [O III] (left), [S III] (middle) and with [Si VI] (right) for the same sample of AGN.

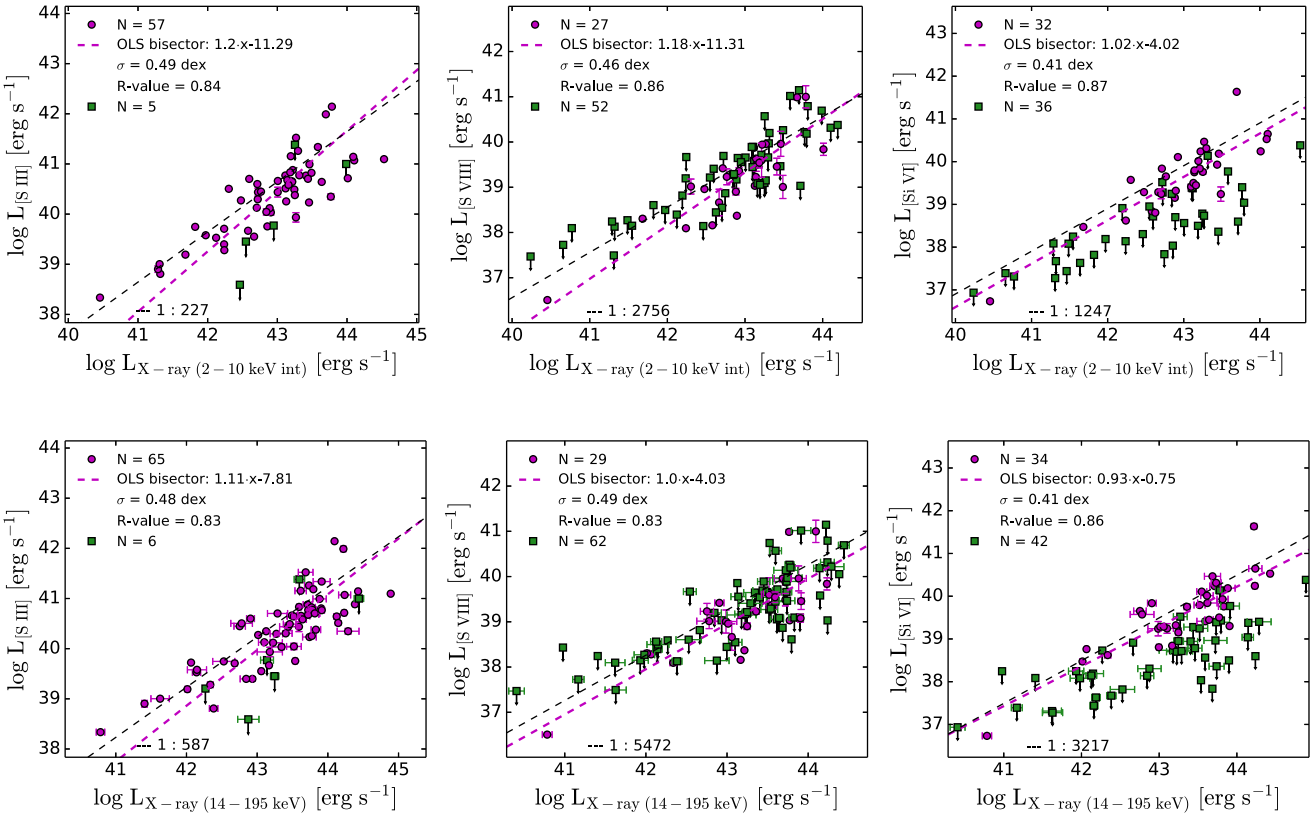

Figure 9. Upper panels: relation of the 2–10-keV X-ray luminosity with [S III] (left), [S VIII] (middle) and [Si VI] (right). The magenta dashed lines show the OLS bisector fit. The black dashed lines have slope 1 and are scaled according to the mean flux ratio. Upper limits (green squares) are not included in the measurements of the OLS bisector fit and mean flux ratio. Lower panels: relation of the 14–195-keV X-ray luminosity (14–195 keV) with [S III] (left), [S VIII] (middle) and [Si VI] (right).

5.2 Hidden BLR

We detected broad lines in 3/33 (9 per cent) Seyfert 2 galaxies in our sample. If we consider also intermediate-class AGN (Seyfert 1.8 and Seyfert 1.9) together with Seyfert 2, we find broad lines in 19/62 AGN (31 per cent). This result is similar to the fraction (32 per cent) found by Onori et al. (2014, 2016). They detected broad emission-line components in Paα, Paβ or He I in 13/41 obscured nearby AGN (Seyfert 1.8, Seyfert 1.9 and Seyfert 2). There are eight objects in common between our sample and their sample. We detected broad lines in 2/8 objects, while they detected broad lines in two additional objects. For these two AGN, we did not detect broad lines because the spectra do not have enough S/N or have telluric features in the Paα and Paβ regions. Also, a previous study by Veilleux et al. (1997) found hidden BLR in 9/33 Seyfert 2 galaxies (27 per cent). Our result suggests that for at least 10 per cent of Seyfert 2 galaxies, we should expect to detect broad lines in the NIR, that can be used to derive a virial measure of $M_{\rm BH}$. We observed that the detection of broad lines in the NIR for Seyfert 2 galaxies is related to lower column densities. All the AGN with hidden BLRs are part of the bottom 11 percentile in $\log N_{\rm H}$. This result suggests that the value of $N_{\rm H}$ can provide an indication of the probability to detect broad lines in the NIR. Two of the AGN with hidden BLR, Mrk 520 and NGC 5231, are in mergers (Koss et al. 2011, 2012), while the third one (NGC 5252) shows signs of tidal material related to a merger (Keel et al. 2015). This suggests that the broad emission lines in the optical are obscured by host galaxy dust and not by the nuclear torus.

We also found that 6/22 (27 per cent) Seyfert 1.9 do not show broad lines in the NIR. In most of these AGN, the broad Hα component is weak as compared to the continuum (EQW[b Hα] < 36 Å), but this is unlikely to be related to dust obscuration as the broad lines are not detected in the NIR. We note that for weak broad lines the NIR has less sensitivity than the optical observations around Hα, unless the lines are significantly obscured.

5.3 AGN diagnostic

We tested the NIR diagnostic diagram on our sample of hard X-ray-selected AGN. Previous studies tested this diagnostic method on samples of AGN (Seyfert 2) and SFGs. They found that Seyfert 2 galaxies are clearly identified as AGN (Rodríguez-Ardila et al. 2004, 2005; Riffel et al. 2013), whereas the sample of SFGs lies both in the SF and in AGN regions of the diagram (Dale et al. 2004; Martins et al. 2013). Only 32/102 (31 per cent) spectra show the emission lines necessary to apply the diagnostic method. We found that 25/102 (25 per cent) objects are identified as AGN and 7/102 (7 per cent) are identified as SFGs. Thus, while it is true that all nine Seyfert 2 AGN with all detected emission lines in our sample were in the AGN region, the NIR diagnostic diagram is not effective for finding AGN in typical surveys because of contamination by SFR galaxies and the difficulty detecting all the emission lines needed for the NIR AGN diagnostic.

5.4 Coronal line emission

We observed that in general the number of CL detections increase with decreasing IP. However, there are some lines that do not follow this trend. For instance, the [Ca VIII] λ2.321-μm line has the lowest IP among the CLs, but we consider it difficult to detect for two reasons. First, [Ca VIII] is located near the red end of the *K* band, and therefore for redshift $z > 0.035$, it falls outside the wavelength range covered by our spectra. Moreover, the [Ca VIII] line is in the same wavelength position of the CO (3–1) absorption line. Therefore the CO (3–1) absorption line can attenuate the strength of the [Ca VIII] line, making more difficult to detect it. Additionally, the [Ca VIII] line can be affected by metallicity effects. There are three CLs ([Al IX], [Si XI] and [S XI]) that are not detected in our spectra. The [Al IX] emission line is affected by metallicity effects and depletion on to dust (Rodríguez-Ardila et al. 2011).

Rodríguez-Ardila et al. (2011) found that the non-detections of CL are associated with either loss of spatial resolution or increasing object distance. CLs are emitted in the nuclear region and they lose contrast with the continuum stellar light in nearby sources. On the other hand, as the redshift increases the CL emission can be diluted by the strong AGN continuum. However, Rodríguez-Ardila et al. (2011) claimed that in some AGN the lack of CL may be genuine: it can be due to a very hard AGN ionizing continuum, without photons with energy below a few keV. Using a survival analysis to compare the CL emission of Seyfert 1 and Seyfert 2 as compared to the bolometric emission, we do find that Seyfert 1 have more CL emission, which may be a consequence of the torus obscuring some of the CL emission.

5.5 Coronal lines and X-ray emission

We found that the scatter in the comparison between the CL flux and hard X-ray flux (14–195 or 2–10 keV) is almost the same as the scatter between [O III] flux and hard X-ray flux. However, the relation of the hard X-ray luminosity with [Si VI] luminosity ($R_{\rm pear} = 0.86$) is stronger than the relation with [O III] ($R_{\rm pear} = 0.73$), based on a Z-test.

In a past study, Rodríguez-Ardila et al. (2011) also found a correlation between the CL emission and X-ray emission from *ROSAT*. They found that the large scatter in the correlation is introduced mostly by the Seyfert 2, while Seyfert 1 follow a narrower trend, with a strong correlation between the absorption-corrected 2–10-keV luminosity and CL luminosity (correlation index of 0.97). We do not observe a stronger correlation between 14–195-keV X-ray flux and CL flux in Seyfert 1 than in Seyfert 2, and this suggests that the weak correlation between CL emission and X-ray is not caused by obscuration.

The condition of the gas in the galaxy can also affect the CL emission. Factors that can influence the strength of the CLs are the gas electron density ($N_{\rm e}$), its temperature and its ionization state. Moreover, the covering factor of the CLR, which is defined by the spatial distribution of the gas and by the angular distribution of the ionizing radiation, can also affect the CL emission (Baskin & Laor 2005). Rodríguez-Ardila et al. (2011) estimated the density of the CLR to be between BLR and NLR. Landt et al. (2015) instead found that the CL gas has a relatively low density of $N_{\rm e} = 10^3$ cm^{-3}. A detailed study of the condition of the gas in the CLR is therefore crucial to quantify the impact of all these factors on the CL emission.

A possible explanation for this scatter remains AGN variability. If CLs are emitted between the BLR and the NLR, we should expect them to be more correlated with the X-ray than [O III]. But if they are located in a region that extends also beyond the inner boundary of the NLR, they can be influenced by variability in a similar way as the NLR. Until now, the exact location of the CLR is controversial. Portilla, Rodríguez-Ardila & Tejeiro (2008) analysed the NIR spectra of a sample of 54 AGN and found that Seyfert 1 show more CLs than Seyfert 2. Their result suggested that CLs are emitted in an extended region and not on the inner surface of the torus. This is in agreement with the study of Rodríguez-Ardila et al. (2006), who found that the size of the CLR extends up to a few hundreds of parsecs. Landt et al. (2015), analysing the CLR in NGC 4151, found instead that extension of the CL gas is beyond the inner face of the torus.

5.6 Outlook for *James Webb Space Telescope* AGN surveys

Our survey provides a comprehensive census and legacy data base of the nearest X-ray-detected AGN with spectroscopic measurements in the NIR. The AGN in the BASS survey serve as a useful low-redshift template for studies of AGN physics, as they have luminosities that are comparable to those of higher redshift ($z > 1$) AGN, detected in pencil-beam, deep X-ray surveys (Koss et al., submitted).

The Near-Infrared Spectrograph (NIRSpec) is an NIR multi-object dispersive spectrograph on board the *James Webb Space Telescope* (*JWST*), capable of simultaneously observing more than 100 slits over the wavelength range of 1–5 μm. The medium resolution mode is expected to provide $R = 1000$, which is similar to the resolution of the spectra presented in this study, and thus sufficient for resolving the NIR CLs. An exposure of 100 000 s is expected to reach a limiting line flux of $\sim 5.7 \times 10^{-19}$ erg cm^{-2} s^{-1} at 2.0 μm with S/N = 10, or $\sim 2 \times 10^{-19}$ erg cm^{-2} s^{-1} with S/N = 3. This is a factor of ∼10 000 times more sensitive than our IRTF programme for the 3σ upper limits of line detection of the [Si VI] line ($\sim 2 \times 10^{-15}$ erg cm^{-2} s^{-1}). Based on the typical scaling factor we found between the [Si VI] and the 2–10-keV emission, of about 1270, this corresponds to an X-ray flux of roughly 2×10^{-16} erg cm^{-2} s^{-1}. This X-ray flux limit, in turn, corresponds to a completeness rate of about 20 per cent (6/30) for the Seyfert 2 sources in our survey. For comparison, the deepest X-ray data in *Chandra* Deep Field South (of 4 Ms) have very similar sensitivities in the hard band (2–8 keV), of $\sim 2 \times 10^{-16}$ erg cm^{-2} s^{-1} at the 20 per cent completeness level (Xue et al. 2011). Thus, deep CL surveys of galaxies using *JWST*/NIRSpec could be as sensitive to AGN as the deepest X-ray surveys. This would be particularly important for detecting heavily obscured (Compton-thick) AGN that are missed by X-ray surveys, and/or nearby low-luminosity AGN for which source confusion is difficult in the X-ray.

6 CONCLUSIONS

The goal of this work was to study the NIR spectroscopic properties of a large sample of nearby hard X-ray-selected AGN. We found the following.

(i) The FWHM of Paβ is similar to the FWHM of Hα and Hβ, if we take into account the emission from Fe multiplets. The FWHM of Paα is smaller on average than the FWHM of the other hydrogen lines, but the difference is not statistically significant.

(ii) AGN with a 'hidden BLR' not observed in optical Balmer lines are the Seyfert 2 with the lowest values of $N_{\rm H}$ in our sample (bottom 11 percentile in $N_{\rm H}$) and show signs of ongoing mergers

Table 8. Stellar velocity dispersion measurements.

ID[a]	$\sigma_{*,\mathrm{CaT}}$ (km s^{-1})	Flag$_{\mathrm{CaT}}$[b]	$\sigma_{*,\mathrm{CO}}$ *K* band (km s^{-1})	Flag$_{\mathrm{CO}}$ *K* band	$\sigma_{*,\mathrm{CO}}$ *H* band (km s^{-1})	Flag$_{\mathrm{CO}}$ *H* band
6	–	9	–	9	–	9
33	–	9	–	9	–	9
116	–	9	207.0 ± 11.9	2	241.4 ± 7.8	1
130	–	9	–	9	–	9
140	–	9	211.8 ± 3.6	1	265.1 ± 12.3	2
157	–	9	–	9	275.0 ± 16.7	2
173	–	9	–	9	–	9
226	–	9	–	9	–	9
266	–	9	–	9	–	9
269	–	9	180.2 ± 7.9	2	187.6 ± 7.9	1

Notes. This table is available in its entirety in a machine-readable form as Supporting Information online. A portion is shown here for guidance regarding its form and content.
[a] *Swift*/BAT 70-month hard X-ray survey ID (http://swift.gsfc.nasa.gov/results/bs70mon/).
[b] Quality flags: 1 = excellent fit with small error ($\langle\Delta\sigma_*\rangle = 6$ km s^{-1}), 2 = larger errors than flag 1 ($\langle\Delta\sigma_*\rangle = 12$ km s^{-1}), but acceptable fit, 3 = bad fit with high S/N, 9 = bad fit.

or tidal features suggesting the obscuration is related to the merger event.

(iii) We measured M_{BH} for the 68 per cent of the AGN in our sample, either from the broad Paschen lines or from the velocity dispersion in the CO band-head.

(iv) Overall, we find that the NIR region is significantly less effective at identifying X-ray-selected AGN compared to emission-line diagnostics in the optical. Only 25 per cent (25/102) of our sample is identified as AGN, whereas 7 per cent (7/102) are classified as SFGs, with the remaining majority of sources having too faint emission lines for classification. While much deeper studies may identify many more spectra in the AGN region, the contamination with star-forming regions is a significant problem.

(v) We found that the relation between [Si VI] and hard X-ray flux is weak (scatter $\sigma = 0.43$ dex, correlation coefficient $R_{\mathrm{pear}} = 0.58$) and not significantly better than the one between [O III] and hard X-ray flux (scatter $\sigma = 0.59$ dex, correlation coefficient $R_{\mathrm{pear}} = 0.50$), based on a Z-test. However, the relation of the hard X-ray luminosity with [Si VI] luminosity ($R_{\mathrm{pear}} = 0.86$) is stronger than the relation with [O III] ($R_{\mathrm{pear}} = 0.74$), based on a Z-test.

Table 9. Black hole mass measurements.

ID[a]	$\log M_{\mathrm{BH}}/\mathrm{M}_\odot$ from Paβ	Flag$_{\mathrm{Pa}\,\beta}$	$\log M_{\mathrm{BH}}/\mathrm{M}_\odot$ from σ_{CO}	Flag$_{\mathrm{CO}}$
6	7.39 ± 0.07	2	–	9
33	–	9	–	9
116	–	9	8.85 ± 0.3	1
130	6.5 ± 0.12	2	–	9
140	–	9	9.03 ± 0.3	2
157	–	9	9.1 ± 0.3	2
173	–	9	–	9
226	–	9	–	9
266	8.19 ± 0.04	2	–	9
269	7.31 ± 0.07	2	8.37 ± 0.3	1

Notes. This table is available in its entirety in a machine-readable form as Supporting Information online. A portion is shown here for guidance regarding its form and content.
[a] *Swift*/BAT 70-month hard X-ray survey ID (http://swift.gsfc.nasa.gov/results/bs70mon/).

ACKNOWLEDGEMENTS

We thank the anonymous referee for the helpful comments. MK acknowledges support from the Swiss National Science Foundation (SNSF) through the Ambizione fellowship grant PZ00P2_154799/1. MK was a visiting astronomer at the Infrared Telescope Facility, which is operated by the University of Hawaii under contract NNH14CK55B with the National Aeronautics and Space Administration (IRTF programmes 2010A-059, 2011A-077, 2011B-104, 2012A-083). The authors wish to recognize and acknowledge the very significant cultural role and reverence that the summit of Mauna Kea has always had within the indigenous Hawaiian community. We are most fortunate to have the opportunity to conduct observations from this mountain. We acknowledge the work that the *Swift*/BAT team has done to make this work possible. The Kitt Peak National Observatory observations were obtained using MD-TAC time as part of the thesis of MK (2008B-0426, 2009A-0287, 2009B-0569) and also through NOAO time in programme 2010A-0447 (PI M. Koss). Kitt Peak National Observatory, National Optical Astronomy Observatory, is operated by the Association of Universities for Research in Astronomy (AURA), Inc., under cooperative agreement with the National Science Foundation. Data from Gemini programmes (GN-2011B-Q-111,GN-2012A-Q-23, GN-2012B-Q-80, GN-2013A-Q-16, GN-2013A-Q-120) were used in this publication. MK would like to thank Dick Joyce at the NOAO for teaching him how to use the FLAMINGOS spectrograph on his first NIR spectroscopy run, the help of John Rayner with SPEX, and Michael Cushing for help with SPEXTOOL. KS gratefully acknowledges support from Swiss National Science Foundation Grant PP00P2_138979/1. CR acknowledges financial support from the CONICYT-Chile 'EMBIGGEN' Anillo (grant ACT1101), FONDECYT 1141218 and Basal-CATA PFB–06/2007. AR-A acknowledges the Conselho Nacional de Desenvolvimento Científico e Tecnológico (CNPq) for partial support to this work (grant 311935/2015-0). RR acknowledges support from CNPq and FAPERGS.

This research made use of ASTROPY, a community-developed core PYTHON package for astronomy (Astropy Collaboration, 2013). This research has made use of the NASA/IPAC Extragalactic Database (NED), which is operated by the Jet Propulsion Laboratory, California Institute of Technology, under contract with the National Aeronautics and Space Administration.

Table 10. Emission lines' flux measurements in the Pa14 region (0.84–0.99 μm) (part 1).

ID[a]	Flag[b]	nFWHM[c] (km s^{-1})	bFWHM[d] (km s^{-1})	Δv[e] (km s^{-1})	O I[f] λ0.8449 μm	b O I	Pa16 λ0.8503 μm	b Pa16	Pa15 λ0.8545 μm	b Pa15
6	2	–	–	–	<10.2	<10.2	<18.6	<18.6	<8.0	<8.0
33	9	–	–	–	<8.2	<8.2	<1.1	<1.1	<2.3	<2.3
116	9	–	–	–	<3.5	<3.5	<7.9	<7.9	<6.4	<6.4
130	2	792 ± 388	–	–	<0.6	<0.6	<0.3	0.7 ± 0.2	0.2 ± 0.3	<0.9
140	9	–	–	–	–	–	–	–	–	–
157	9	–	–	–	–	–	–	–	–	–
173	9	–	–	–	–	–	–	–	–	–
226	−1	–	–	–	–	–	–	–	–	–
266	9	–	3299 ± 999	–	67.9 ± 22.1	67.9 ± 22.1	8.4 ± 1.1	67.9 ± 19.9	<28.4	60.7 ± 15.3
269	9	–	–	–	–	–	–	–	–	–

Notes. This table is available in its entirety in a machine-readable form as Supporting Information online. A portion is shown here for guidance regarding its form and content.
[a]*Swift*-BAT 70-month hard X-ray survey ID (http://swift.gsfc.nasa.gov/results/bs70mon/).
[b]Spectral fitting quality flags: 1 = good fit, 2 = acceptable fit, 9 = bad fit, −1 = lack of spectral coverage.
[c, d]nFWHM: FWHM of the narrow lines. bFWHM: FWHM of the broad lines. The FWHM are not corrected for the instrumental resolution.
[e]Velocity offset of the broad components with respect to the systemic redshift.
[f]Emission lines' fluxes are in units of 10^{-15} erg s^{-1} cm^{-2}. Negative numbers indicate upper limits.

Table 11. Emission lines' flux measurements in the Pa14 region (0.84–0.99 μm) (part 2).

ID[a]	Flag[b]	Pa14[c] λ0.8600 μm	b Pa14	Pa13 λ0.8665 μm	b Pa13	Pa12 λ0.8750 μm	b Pa12	Pa11 λ0.8863 μm	b Pa11
6	2	<5.0	<5.0	<5.8	<5.8	<6.8	<6.8	8.8 ± 0.9	<8.7
33	9	<4.8	<4.8	<4.4	<4.4	<2.1	<2.1	2.0 ± 0.9	<2.0
116	9	<5.8	<5.8	<5.4	<5.4	<5.2	<5.2	<6.0	<6.0
130	2	<0.3	<0.3	0.3 ± 0.0	<0.2	<0.3	<0.3	<0.3	<0.3
140	9	–	–	–	–	–	–	–	–
157	9	–	–	–	–	–	–	–	–
173	9	–	–	–	–	–	–	–	–
226	−1	–	–	–	–	–	–	–	–
266	9	<18.1	31.0 ± 4.2	<11.5	<11.5	<12.1	<12.1	<6.2	<6.2
269	9	–	–	–	–	–	–	–	–

Notes. This table is available in its entirety in a machine-readable form as Supporting Information online. A portion is shown here for guidance regarding its form and content.
[a]*Swift*/BAT 70-month hard X-ray survey ID (http://swift.gsfc.nasa.gov/results/bs70mon/).
[b]Spectral fitting quality flags: 1 = good fit, 2 = acceptable fit, 9 = bad fit, −1 = lack of spectral coverage.
[c]Emission lines' fluxes are in units of 10^{-15} erg s^{-1} cm^{-2}. Negative numbers indicate upper limits.

Table 12. Emission lines' flux measurements in the Pa ζ region (0.90–0.96 μm).

ID[a]	Flag[b]	nFWHM[c] (km s^{-1})	bFWHM[d] (km s^{-1})	Δv[e] (km s^{-1})	[S III][f] λ0.9069 μm	[S III] λ0.9531 μm	Pa10 λ0.9016 μm	b Pa10	Pa ζ λ0.9229 μm	b Pa ζ	Pa ϵ λ0.9546 μm	b Pa ϵ
6	2	605 ± 40	3153 ± 62	−457 ± 60	9.8 ± 0.4	19.7 ± 1.0	8.5 ± 1.0	15.0 ± 13.2	<18.7	75.6 ± 1.0	7.5 ± 0.7	53.5 ± 2.0
33	2	641 ± 5	–	–	48.7 ± 0.7	123.0 ± 1.3	<6.8	–	<5.3	–	<47.8	–
116	2	654 ± 42	–	–	7.5 ± 0.3	16.6 ± 1.8	<6.1	–	<6.0	–	<5.8	–
130	9	–	–	–	0.5 ± 0.1	<0.7	<0.5	<2.7	0.4 ± 0.1	<2.0	0.7 ± 0.1	<1.9
140	9	676 ± 32	4683 ± 208	–	28.9 ± 1.1	39.1 ± 1.4	<21.6	–	<42.8	90.5 ± 2.8	<50.8	66.3 ± 2.5
157	9	821 ± 77	–	–	3.0 ± 0.3	8.2 ± 0.9	<0.8	–	<3.1	–	<1.9	–
173	2	1257 ± 1	–	–	72.1 ± 1.7	180.0 ± 11.8	<25.8	–	<2.5	–	<86.4	–
226	2	314 ± 12	3146 ± 95	114 ± 70	<4.0	30.0 ± 1.2	<3.7	<50.9	<7.9	106.0 ± 2.5	<5.5	98.5 ± 4.9
266	9	524 ± 40	5166 ± 80	–	12.0 ± 1.0	22.9 ± 1.5	<7.5	<79.0	<5.3	228.0 ± 4.2	<8.4	149.0 ± 3.2
269	9	534 ± 11	–	–	16.5 ± 1.1	34.2 ± 1.0	<1.8	<19.2	<8.3	<88.3	<16.3	28.2 ± 1.5

Notes. This table is available in its entirety in a machine-readable form as Supporting Information online. A portion is shown here for guidance regarding its form and content.
[a]*Swift*/BAT 70-month hard X-ray survey ID (http://swift.gsfc.nasa.gov/results/bs70mon/).
[b]Spectral fitting quality flags: 1 = good fit, 2 = acceptable fit, 9 = bad fit, −1 = lack of spectral coverage.
[c, d]nFWHM: FWHM of the narrow lines. bFWHM: FWHM of the broad lines. The FWHM are not corrected for the instrumental resolution.
[e]Velocity offset of the broad components with respect to the systemic redshift.
[f]Emission lines' fluxes are in units of 10^{-15} erg s^{-1} cm^{-2}. Negative numbers indicate upper limits.

Table 13. Emission lines' flux measurements in the Pa δ region (0.96–1.04 μm) (part 1).

ID[a]	Flag[b]	nFWHM[c] (km s^{-1})	bFWHM[d] (km s^{-1})	Δv[e] (km s^{-1})	[C I][f] λ0.9827 μm	[C I] λ0.9853 μm	[S VIII] λ0.9915 μm	[Fe II] λ0.9999 μm	He II λ1.0126 μm	[S II] λ1.0290 μm
6	3	780 ± 598	4245 ± 532	–	<3.6	<2.9	3.4 ± 8.5	<23.0	3.1 ± 7.6	<4.0
33	3	660 ± 41	–	–	1.5 ± 22.5	3.9 ± 21.5	2.3 ± 20.0	<0.8	3.6 ± 22.0	5.0 ± 15.1
116	3	596 ± 22	–	–	<4.5	1.9 ± 1.8	<3.0	<1.9	2.1 ± 2.2	<3.5
130	2	5158 ± 1	4899 ± 4	−573 ± 30	<0.1	<0.1	<0.2	1.6 ± 0.4	<0.2	<0.1
140	3	800 ± 51	–	–	<26.8	11.3 ± 3.1	<8.0	<7.7	<11.5	11.5 ± 7.3
157	2	804 ± 106	–	–	<2.2	1.6 ± 1.2	<0.5	<0.6	<1.7	<1.4
173	3	1372 ± 154	–	–	<28.7	21.6 ± 28.8	<0.5	<4.0	<4.7	24.6 ± 34.1
226	2	335 ± 67	2837 ± 832	−35 ± 6	<4.0	<7.8	<4.4	<23.8	4.4 ± 5.8	<4.8
266	2	590 ± 84	5528 ± 121	−85 ± 15	<4.8	<12.6	<25.0	<22.3	9.8 ± 12.1	<7.7
269	3	624 ± 26	5910 ± 54	–	<5.4	2.0 ± 2.3	2.2 ± 1.9	<0.7	3.7 ± 1.2	<3.7

Notes. This table is available in its entirety in a machine-readable form as Supporting Information online. A portion is shown here for guidance regarding its form and content.
[a]*Swift*/BAT 70-month hard X-ray survey ID (http://swift.gsfc.nasa.gov/results/bs70mon/).
[b]Spectral fitting quality flags: 1 = good fit, 2 = acceptable fit, 9 = bad fit, −1 = lack of spectral coverage.
[c, d]nFWHM: FWHM of the narrow lines. bFWHM: FWHM of the broad lines. The FWHM are not corrected for the instrumental resolution.
[e]Velocity offset of the broad components with respect to the systemic redshift.
[f]Emission lines' fluxes are in units of 10^{-15} erg s^{-1} cm^{-2}. Negative numbers indicate upper limits.

Table 14. Emission lines' flux measurements in the Pa δ region (0.96–1.04 μm) (part 2).

ID[a]	Flag[b]	[S II][c] λ1.0320 μm	[S II] λ1.0336 μm	[S II] λ1.0370 μm	[N I] λ1.0404 μm	Pa δ λ1.0049 μm	b Pa δ
6	3	<1.4	<2.9	<2.8	<3.5	13.8 ± 8.2	110.0 ± 63.7
33	3	6.3 ± 12.6	5.0 ± 15.6	1.5 ± 15.6	1.4 ± 21.4	2.4 ± 13.4	–
116	3	1.3 ± 1.8	<2.3	<4.2	<2.3	<2.8	–
130	2	<0.1	<0.1	<0.1	<0.1	0.4 ± 0.2	1.6 ± 1.1
140	3	12.1 ± 6.6	5.8 ± 6.8	<9.2	7.3 ± 5.8	<11.1	–
157	2	<2.0	<1.8	<2.9	<1.6	<0.7	–
173	3	29.5 ± 13.6	32.5 ± 23.7	14.3 ± 27.5	26.2 ± 16.1	3.3 ± 22.5	–
226	2	<6.1	<6.7	<6.9	<11.5	<3.7	102.0 ± 74.9
266	2	<3.4	<4.7	<3.6	<4.2	<4.4	343.0 ± 8.3
269	3	1.8 ± 3.0	<1.9	<4.3	<1.0	<1.8	35.7 ± 29.4

Notes. This table is available in its entirety in a machine-readable form as Supporting Information online. A portion is shown here for guidance regarding its form and content.
[a]*Swift*/BAT 70-month hard X-ray survey ID (http://swift.gsfc.nasa.gov/results/bs70mon/).
[b]Spectral fitting quality flags: 1 = good fit, 2 = acceptable fit, 9 = bad fit, −1 = lack of spectral coverage.
[c]Emission lines' fluxes are in units of 10^{-15} erg s^{-1} cm^{-2}. Negative numbers indicate upper limits.

Table 15. Emission lines' flux measurements in the Paγ region (1.04–1.15 μm).

ID[a]	Flag[b]	nFWHM[c] (km s^{-1})	bFWHM[d] (km s^{-1})	Δv[e] (km s^{-1})	[Fe II][f] λ1.0500 μm	[Fe XIII] λ1.0747 μm	[Fe II] λ1.0370 μm	He I λ1.0404 μm	b He I	Paγ λ1.0938 μm	b Paγ	O I λ1.1287 μm	b O I
6	2	–	–	–	7.7 ± 0.2	<22.4	<3.4	138.0 ± 0.6	234.0 ± 1.1	43.6 ± 0.4	<90.1	23.4 ± 0.6	<14.2
33	9	–	–	–	<3.0	<0.7	<1.2	50.3 ± 1.1	20.4 ± 1.2	4.3 ± 0.2	–	<0.4	–
116	2	–	–	–	<1.8	<8.4	<2.0	13.0 ± 0.5	59.0 ± 1.1	<10.1	–	<2.0	–
130	2	795 ± 1	2045 ± 42	−63 ± 3	0.2 ± 0.1	0.2 ± 0.1	<0.2	1.0 ± 0.1	2.5 ± 0.1	0.3 ± 0.1	1.0 ± 0.1	0.2 ± 0.1	0.4 ± 0.1
140	9	–	–	–	<10.0	<23.1	<8.2	80.1 ± 23.3	–	<34.1	–	<11.9	–
157	9	–	–	–	<0.4	<0.5	<1.1	<1.0	–	<2.8	–	<2.6	–
173	9	–	2684 ± 16	–	<1.5	<74.7	<1.2	102.0 ± 2.2	474.0 ± 2.9	12.2 ± 1.1	54.3 ± 2.4	<4.4	–
226	2	–	4571 ± 232	63 ± 3	7.1 ± 0.7	<36.7	<2.8	169.0 ± 10.9	538.0 ± 7.6	15.9 ± 4.2	161.0 ± 10.9	13.8 ± 2.9	<58.4
266	2	–	5581 ± 221	136 ± 19	<5.0	<87.6	<14.1	93.0 ± 9.6	1020.0 ± 64.7	<72.7	279.0 ± 70.4	<4.8	–
269	2	–	–	–	<2.2	<10.6	<2.2	58.9 ± 0.6	143.0 ± 1.6	<14.8	–	<0.4	–

Notes. This table is available in its entirety in a machine-readable form as Supporting Information online. A portion is shown here for guidance regarding its form and content.
[a]*Swift*/BAT 70-month hard X-ray survey ID (http://swift.gsfc.nasa.gov/results/bs70mon/).
[b]Spectral fitting quality flags: 1 = good fit, 2 = acceptable fit, 9 = bad fit, −1 = lack of spectral coverage.
[c, d]nFWHM: FWHM of the narrow lines. bFWHM: FWHM of the broad lines. The FWHM are not corrected for the instrumental resolution.
[e]Velocity offset of the broad components with respect to the systemic redshift.
[f]Emission lines' fluxes are in units of 10^{-15} erg s^{-1} cm^{-2}. Negative numbers indicate upper limits.

Table 16. Emission lines' flux measurements in the Paβ region (1.15–1.30 μm).

ID[a]	Flag[b]	nFWHM[c] (km s^{-1})	bFWHM[d] (km s^{-1})	b Δv[e] (km s^{-1})	He II[f] λ1.1620 μm	[P II] λ1.1886 μm	[S IX] λ1.2520 μm	[Fe II] λ1.2570 μm	[Fe II] λ1.2788 μm	[Fe II] λ1.2950 μm	[Fe II] λ1.3201 μm	Paβ λ1.2818 μm	b Paβ
6	2	–	2741 ± 67	−133 ± 9	<0.8	<1.2	3.7 ± 0.2	1.9 ± 1.0	17.8 ± 0.7	1.7 ± 1.7	<8.9	36.7 ± 0.9	117.0 ± 1.2
33	2	644 ± 285	–	42 ± 6	<0.7	3.0 ± 0.6	<2.3	12.1 ± 0.1	<10.6	<3.0	2.6 ± 0.8	11.3 ± 0.2	–
116	9	635 ± 246	–	–	<1.9	<2.1	<1.5	<0.9	3.4 ± 0.3	<2.5	2.7 ± 0.6	<1.8	–
130	2	–	3572 ± 200	−375 ± 28	<0.1	<0.1	<0.2	<0.1	<1.8	<0.1	<0.2	1.0 ± 0.1	0.9 ± 0.1
140	3	788 ± 381	–	–	<6.8	<4.1	<21.2	31.1 ± 0.9	10.7 ± 2.0	<6.2	10.0 ± 2.8	<20.6	–
157	9	–	–	–	<0.9	<0.4	<0.2	<0.3	<0.4	<0.8	<0.1	<1.3	–
173	3	518 ± 1	518 ± 1	–	<1.2	11.4 ± 0.2	<15.8	50.6 ± 0.2	<25.6	<0.9	11.6 ± 0.4	12.6 ± 7.7	51.2 ± 25.8
226	3	–	2842 ± 29	–	<1.4	<0.3	6.0 ± 0.4	3.3 ± 0.8	<34.8	3.8 ± 2.5	<62.5	<9.3	239.0 ± 2.7
266	2	507 ± 1	4864 ± 15	362 ± 6	<2.4	<2.6	<3.3	4.0 ± 0.7	<22.6	<40.5	26.2 ± 0.9	<8.6	496.0 ± 1.3
269	2	–	4379 ± 99	−111 ± 36	<0.6	<0.6	<1.4	4.6 ± 0.2	<7.4	<3.9	<1.3	3.4 ± 0.3	48.9 ± 0.4

Notes. This table is available in its entirety in a machine-readable form as Supporting Information online. A portion is shown here for guidance regarding its form and content.
[a]*Swift*/BAT 70-month hard X-ray survey ID (http://swift.gsfc.nasa.gov/results/bs70mon/).
[b]Spectral fitting quality flags: 1 = good fit, 2 = acceptable fit, 9 = bad fit, −1 = lack of spectral coverage.
[c, d]nFWHM: FWHM of the narrow lines. bFWHM: FWHM of the broad lines. The FWHM are not corrected for the instrumental resolution.
[e]Velocity offset of the broad components with respect to the systemic redshift.
[f]Emission lines' fluxes are in units of 10^{-15} erg s^{-1} cm^{-2}. Negative numbers indicate upper limits.

Table 17. Emission lines' flux measurements in the Br10 region (1.30–1.80 μm).

ID[a]	Flag[b]	nFWHM[c] (km s^{-1})	bFWHM[d] (km s^{-1})	b Δv[e] (km s^{-1})	[Si X][f] λ1.4300 μm	[Fe II] λ1.5339 μm	[Fe II] λ1.6436 μm	[Fe II] λ1.6807 μm	Br10 λ1.7367 μm	b Br10	Br11 λ1.6811 μm	b Br11
6	9	–	–	–	<5.1	<2.8	4.3 ± 0.4	<1.2	<1.2	<1.2	4.2 ± 0.7	<1.1
33	1	763 ± 1	–	–	2.0 ± 0.2	2.0 ± 0.2	9.4 ± 0.1	<0.9	<1.1	<1.1	<1.1	<1.1
116	9	–	–	–	<2.0	<1.9	<2.4	<1.5	<1.8	<1.8	<0.5	<0.5
130	9	–	–	–	<0.1	<0.1	<0.1	<0.1	<0.1	<0.1	<0.1	<0.1
140	9	–	–	–	<8.4	<7.3	27.0 ± 1.6	<10.2	<11.8	<11.8	<12.3	<12.3
157	9	–	–	–	<0.5	<0.5	<1.5	<0.4	<0.5	<0.5	<0.5	<0.5
173	2	–	–	–	<1.0	6.9 ± 0.2	49.2 ± 0.4	<5.0	<5.4	<5.4	<1.5	<1.5
226	9	–	–	–	<3.8	<1.7	<0.8	<2.5	<2.2	<2.2	<2.3	<2.3
266	9	–	–	–	<8.2	<5.6	<1.3	<2.4	<2.7	<2.7	<2.8	<2.8
269	9	–	–	–	<2.6	<0.5	<4.6	<3.7	<4.0	<4.0	<1.0	<1.0

Notes. This table is available in its entirety in a machine-readable form as Supporting Information online. A portion is shown here for guidance regarding its form and content.
[a]*Swift*/BAT 70-month hard X-ray survey ID (http://swift.gsfc.nasa.gov/results/bs70mon/).
[b]Spectral fitting quality flags: 1 = good fit, 2 = acceptable fit, 9 = bad fit, −1 = lack of spectral coverage.
[c, d]nFWHM: FWHM of the narrow lines. bFWHM: FWHM of the broad lines. The FWHM are not corrected for the instrumental resolution.
[e]Velocity offset of the broad components with respect to the systemic redshift.
[f]Emission lines' fluxes are in units of 10^{-15} erg s^{-1} cm^{-2}. Negative numbers indicate upper limits.

Table 18. Emission lines' flux measurements in the Paα region (1.80–2.00 μm).

ID[a]	Flag[b]	nFWHM[c] (km s^{-1})	bFWHM[d] (km s^{-1})	b Δv[e] (km s^{-1})	[Si XI][f] λ1.9320 μm	H_2 λ1.9564 μm	[Si VI] λ1.9620 μm	Paα λ1.8751 μm	b Paα	Br δ λ1.9446 μm	b Br δ
6	2	374 ± 1	1386 ± 16	−145 ± 8	<2.1	<7.8	<0.4	27.3 ± 1.3	127.0 ± 1.7	8.6 ± 1.1	<5.6
33	3	–	–	–	<0.1	<3.0	4.1 ± 0.2	42.6 ± 0.2	<33.5	<0.3	<0.3
116	9	–	4659 ± 290	–	<0.5	–	<1.2	<1.4	30.1 ± 1.4	<0.2	<0.2
130	9	374 ± 13	–	–	<0.2	<0.1	<0.3	0.7 ± 0.1	<0.2	<0.1	<0.1
140	9	–	–	–	<4.7	–	<3.0	24.7 ± 1.0	<11.8	<8.5	<8.5
157	9	–	–	–	<0.7	–	<0.2	<1.6	<1.6	<0.4	<0.4
173	3	–	2799 ± 43	–	<1.2	–	<3.2	44.9 ± 0.5	146.0 ± 0.9	<0.8	66.6 ± 24.1
226	2	–	2606 ± 16	372 ± 8	<1.6	<1.0	13.2 ± 2.0	12.5 ± 0.7	336.0 ± 2.0	<5.2	<5.2
266	3	953 ± 59	4633 ± 18	–	<7.0	24.8 ± 2.0	20.2 ± 1.4	<12.7	678.0 ± 2.4	<7.9	69.4 ± 2.0
269	2	432 ± 82	3954 ± 76	139 ± 30	<0.3	2.6 ± 0.5	4.3 ± 0.4	20.7 ± 0.3	58.3 ± 1.0	<0.1	<0.1

Notes. This table is available in its entirety in a machine-readable form as Supporting Information online. A portion is shown here for guidance regarding its form and content.
[a]*Swift*/BAT 70-month hard X-ray survey ID (http://swift.gsfc.nasa.gov/results/bs70mon/).
[b]Spectral fitting quality flags: 1 = good fit, 2 = acceptable fit, 9 = bad fit, −1 = lack of spectral coverage.
[c, d]nFWHM: FWHM of the narrow lines. bFWHM: FWHM of the broad lines. The FWHM are not corrected for the instrumental resolution.
[e]Velocity offset of the broad component with respect to the systemic redshift.
[f]Emission lines' fluxes are in units of 10^{-15} erg s^{-1} cm^{-2}. Negative numbers indicate upper limits.

Table 19. Emission lines' flux measurements in the Brγ region (2.00–2.40 μm).

ID[a]	Flag[b]	nFWHM[c] (km s^{-1})	bFWHM[d] (km s^{-1})	b Δv[e] (km s^{-1})	H_2[f] λ2.0330 μm	[Al IX] λ2.0400 μm	He I λ2.0580 μm	H_2 λ2.1213 μm	H_2 λ2.2227 μm	[Ca VIII] λ2.3210 μm	H_2 λ2.2467 μm	Brγ λ2.1655 μm	b Brγ
6	2	–	5592 ± 647	−110 ± 33	<0.5	<1.0	3.8 ± 0.9	<0.3	<0.9	<2.0	<0.6	16.9 ± 1.4	16.4 ± 7.4
33	2	442 ± 33	–	–	0.8 ± 0.3	<0.5	<0.7	1.8 ± 0.1	<0.4	<0.5	<0.8	1.5 ± 0.2	<0.2
116	9	–	–	–	<0.7	<0.3	<0.1	<0.7	<0.3	<1.9	<0.2	<2.0	<0.1
130	9	–	–	–	<0.1	<0.1	<0.1	<0.1	<0.1	<0.1	<0.1	0.3 ± 0.1	<0.1
140	2	–	–	–	<2.9	<0.9	<1.4	3.6 ± 0.2	<1.8	<12.1	<0.6	<12.2	<2.6
157	9	515 ± 38	–	–	0.5 ± 0.3	<0.1	<0.1	0.8 ± 0.1	<0.2	<0.8	<0.1	<0.8	<0.2
173	2	534 ± 7	–	–	14.8 ± 0.6	<3.1	3.6 ± 1.2	42.9 ± 0.7	10.9 ± 0.3	<0.2	4.0 ± 1.7	<0.2	<0.1
226	9	–	–	–	<0.7	<1.1	<0.2	<0.4	<1.4	<1.4	<2.7	<1.4	<4.6
266	2	–	5171 ± 183	110 ± 1	<3.1	<1.4	<1.4	<2.3	<1.8	<2.0	3.8 ± 24.2	<2.1	72.4 ± 1.8
269	2	–	5758 ± 286	63 ± 18	<0.8	<0.3	<0.7	1.4 ± 0.1	<0.5	<2.9	<0.3	0.8 ± 0.7	11.6 ± 3.4

Notes. This table is available in its entirety in a machine-readable form as Supporting Information online. A portion is shown here for guidance regarding its form and content.
[a]*Swift*/BAT 70-month hard X-ray survey ID (http://swift.gsfc.nasa.gov/results/bs70mon/).
[b]Spectral fitting quality flags: 1 = good fit, 2 = acceptable fit, 9 = bad fit, −1 = lack of spectral coverage.
[c, d]nFWHM: FWHM of the narrow lines. bFWHM: FWHM of the broad lines. The FWHM are not corrected for the instrumental resolution.
[e]Velocity offset of the broad component with respect to the systemic redshift.
[f]Emission lines' fluxes are in units of 10^{-15} erg s^{-1} cm^{-2}. Negative numbers indicate upper limits.

REFERENCES

Baskin A., Laor A., 2005, MNRAS, 358, 1043
Baumgartner W. H., Tueller J., Markwardt C. B., Skinner G. K., Barthelmy S., Mushotzky R. F., Evans P. A., Gehrels N., 2013, ApJS, 207, 19
Bentz M. C., Katz S., 2015, PASP, 127, 67
Berney S. et al., 2015, MNRAS, 454, 3622
Black J. H., van Dishoeck E. F., 1987, ApJ, 322, 412
Boroson T. A., Green R. F., 1992, ApJS, 80, 109
Cappellari M., Emsellem E., 2004, PASP, 116, 138
Cenarro A. J., Cardiel N., Gorgas J., Peletier R. F., Vazdekis A., Prada F., 2001, MNRAS, 326, 959
Colina L. et al., 2015, A&A, 578, A48
Crenshaw D. M., Kraemer S. B., 2005, ApJ, 625, 680
Cushing M. C., Vacca W. D., Rayner J. T., 2004, PASP, 116, 362
Cushing M. C., Rayner J. T., Vacca W. D., 2005, ApJ, 623, 1115
Cusumano G. et al., 2010, A&A, 524, A64
Dale D. A. et al., 2004, ApJ, 601, 813
Dasyra K. M. et al., 2006a, ApJ, 638, 745
Dasyra K. M. et al., 2006b, ApJ, 651, 835
Dasyra K. M. et al., 2007, ApJ, 657, 102
De Robertis M., 1985, ApJ, 289, 67
Elias J. H., Joyce R. R., Liang M., Muller G. P., Hileman E. A., George J. R., 2006, in McLean I. S., Iye M., eds, Proc. SPIE Conf. Ser. Vol. 6269, Ground-based and Airborne Instrumentation for Astronomy. SPIE, Bellingham, p. 62694C
Elston R., 1998, in Fowler A. M., ed., Proc. SPIE Conf. Ser. Vol. 3354, Infrared Astronomical Instrumentation. SPIE, Bellingham, p. 404
Feigelson E. D., Nelson P. I., 1985, ApJ, 293, 192
Ferrarese L., Merritt D., 2000, ApJ, 539, L9
Ginsburg A., Mirocha J., 2011, Astrophysics Source Code Library, record ascl:1109.001
Graham A. W., Onken C. A., Athanassoula E., Combes F., 2011, MNRAS, 412, 2211
Greene J. E. et al., 2010, ApJ, 723, 409
Gültekin K. et al., 2009, ApJ, 698, 198
Hollenbach D., McKee C. F., 1989, ApJ, 342, 306
Isobe T., Feigelson E. D., Akritas M. G., Babu G. J., 1990, ApJ, 364, 104
Kang W.-R., Woo J.-H., Schulze A., Riechers D. A., Kim S. C., Park D., Smolcic V., 2013, ApJ, 767, 26
Keel W. C. et al., 2015, AJ, 149, 155
Kim D., Im M., Kim M., 2010, ApJ, 724, 386
Kormendy J., Ho L. C., 2013, ARA&A, 51, 511
Koss M., Mushotzky R., Veilleux S., Winter L. M., Baumgartner W., Tueller J., Gehrels N., Valencic L., 2011, ApJ, 739, 57
Koss M., Mushotzky R., Treister E., Veilleux S., Vasudevan R., Trippe M., 2012, ApJ, 746, L22
Koss M. J. et al., 2016, ApJ, 825, 85
La Franca F. et al., 2015, MNRAS, 449, 1526
Landt H., Bentz M. C., Ward M. J., Elvis M., Peterson B. M., Korista K. T., Karovska M., 2008, ApJS, 174, 282
Landt H., Bentz M. C., Peterson B. M., Elvis M., Ward M. J., Korista K. T., Karovska M., 2011a, MNRAS, 413, L106
Landt H., Elvis M., Ward M. J., Bentz M. C., Korista K. T., Karovska M., 2011b, MNRAS, 414, 218
Landt H., Ward M. J., Peterson B. M., Bentz M. C., Elvis M., Korista K. T., Karovska M., 2013, MNRAS, 432, 113
Landt H., Ward M. J., Steenbrugge K. C., Ferland G. J., 2015, MNRAS, 449, 3795
Larkin J. E., Armus L., Knop R. A., Soifer B. T., Matthews K., 1998, ApJS, 114, 59
McConnell N. J., Ma C.-P., 2012, ApJ, 764, 184
Maloney P. R., Hollenbach D. J., Tielens A. G. G. M., 1996, ApJ, 466, 561
Martins L. P., Rodríguez-Ardila A., Diniz S., Gruenwald R., de Souza R., 2013, MNRAS, 431, 1823
Marziani P., Sulentic J. W., Dultzin-Hacyan D., Calvani M., Moles M., 1996, ApJS, 104, 37
Mason R. E. et al., 2015, ApJS, 217, 13
Mazzalay X., Rodríguez-Ardila A., Komossa S., 2010, MNRAS, 405, 1315
Merritt D., 1997, AJ, 114, 228
Müller-Sánchez F., Prieto M. A., Hicks E. K. S., Vives-Arias H., Davies R. I., Malkan M., Tacconi L. J., Genzel R., 2011, ApJ, 739, 69
Netzer H., Laor A., 1993, ApJ, 404, L51
Netzer H., Mainieri V., Rosati P., Trakhtenbrot B., 2006, A&A, 453, 525
Onori F. et al., 2014, in Caraveo P., D'Avanzo P., Gehrels N., Tagliaferri G., eds, Proc. Science, Swift: 10 Years of Discovery (SWIFT 10). p. 153
Onori F. et al., 2016, MNRAS, 464, 1783
Osterbrock D. E., 1981, ApJ, 249, 462
Peterson B. M., 2014, Space Sci. Rev., 183, 253
Portilla J. G., Rodríguez-Ardila A., Tejeiro J. M., 2008, Rev. Mex. Astron. Astrofis. Ser. Conf., 32, 80
Rayner J. T., Toomey D. W., Onaka P. M., Denault A. J., Stahlberger W. E., Vacca W. D., Cushing M. C., Wang S., 2003, PASP, 115, 362
Rayner J. T., Cushing M. C., Vacca W. D., 2009, ApJS, 185, 289
Ricci C., Ueda Y., Koss M. J., Trakhtenbrot B., Bauer F. E., Gandhi P., 2015, ApJ, 815, L13
Ricci F., La Franca F., Onori F., Bianchi S., 2016, preprint (arXiv:1610.03490)
Riffel R., Rodríguez-Ardila A., Pastoriza M. G., 2006, A&A, 457, 61
Riffel R., Rodríguez-Ardila A., Aleman I., Brotherton M. S., Pastoriza M. G., Bonatto C. J., Dors O. L., Jr, 2013, MNRAS, 430, 2002
Riffel R. A. et al., 2015, MNRAS, 446, 2823
Röck B., Vazdekis A., Peletier R. F., Knapen J. H., Falcón-Barroso J., 2015, MNRAS, 449, 2853
Röck B., Vazdekis A., Ricciardelli E., Peletier R. F., Knapen J. H., Falcón-Barroso J., 2016, A&A, 589, A73
Rodríguez-Ardila A., Viegas S. M., Pastoriza M. G., Prato L., 2002, ApJ, 579, 214
Rodríguez-Ardila A., Pastoriza M. G., Viegas S., Sigut T. A. A., Pradhan A. K., 2004, A&A, 425, 457
Rodríguez-Ardila A., Riffel R., Pastoriza M. G., 2005, MNRAS, 364, 1041
Rodríguez-Ardila A., Prieto M. A., Viegas S., Gruenwald R., 2006, ApJ, 653, 1098
Rodríguez-Ardila A., Prieto M. A., Portilla J. G., Tejeiro J. M., 2011, ApJ, 743, 100
Rothberg B., Fischer J., 2010, ApJ, 712, 318
Rothberg B., Fischer J., Rodrigues M., Sanders D. B., 2013, ApJ, 767, 72
Sánchez-Blázquez P. et al., 2006, MNRAS, 371, 703
Schawinski K., Koss M., Berney S., Sartori L. F., 2015, MNRAS, 451, 2517
Shen Y., 2013, Bull. Astron. Soc. India, 41, 61
Shen Y. et al., 2016, ApJ, 831, 7
Smith K. L., Koss M., Mushotzky R. F., 2014, ApJ, 794, 112
Trakhtenbrot B., Netzer H., 2012, MNRAS, 427, 3081
Tremaine S. et al., 2002, ApJ, 574, 740
Ueda Y. et al., 2015, ApJ, 815, 1
Vacca W. D., Cushing M. C., Rayner J. T., 2002, PASP, 115, 389
Vasudevan R. V., Fabian A. C., 2009, MNRAS, 392, 1124
Vazdekis A., Sánchez-Blázquez P., Falcón-Barroso J., Cenarro A. J., Beasley M. A., Cardiel N., Gorgas J., Peletier R. F., 2010, MNRAS, 404, 1639
Vazdekis A., Ricciardelli E., Cenarro A. J., Rivero-González J. G., Díaz-García L. A., Falcón-Barroso J., 2012, MNRAS, 424, 157
Veilleux S., 2002, in Green R. F., Khachikian E. Ye., Sanders D. B., eds, ASP Conf. Ser. Vol. 284, IAU Colloq. 184: AGN Surveys. Astron. Soc. Pac., San Francisco, p. 111
Veilleux S., Goodrich R. W., Hill G. J., 1997, ApJ, 477, 631
Veron P., Goncalves A. C., Veron-Cetty M. P., 2002, A&A, 384, 826
Winge C., Riffel R. A., Storchi-Bergmann T., 2009, ApJS, 185, 186
Woo J.-H., Schulze A., Park D., Kang W.-R., Kim S. C., Riechers D. A., 2013, ApJ, 772, 49
Xue Y. Q. et al., 2011, ApJS, 195, 10

SUPPORTING INFORMATION

Supplementary data are available at *MNRAS* online.

Table_8_BHmass.txt
Table_9_sigma.txt
Table_10_Pa14.txt
Table_11_Pa14_2.txt
Table_12_Pazeta.txt
Table_13_Padelta.txt
Table_14_Pa_delta_2.txt
Table_15_Pagamma.txt
Table_16_Pabeta.txt
Table_17_Br10.txt
Table_18_Paalpha.txt
Table_19_Brgamma.txt

Please note: Oxford University Press is not responsible for the content or functionality of any supporting materials supplied by the authors. Any queries (other than missing material) should be directed to the corresponding author for the article.

APPENDIX A

Here, we provide additional information about the spectra and fitting. Plots of each of the new spectra obtained in the observing programmes on SpeX and FLAMINGOS are found in Figs. A1–A3. In Section A1, we report a list of the emission and absorption lines present in the NIR range (0.8–2.4 μm). In the next section, we show an example of PPXF absorption-line fitting. In Section A2, we also perform a variety of checks comparing our velocity dispersion measurements obtained from different spectral region in the NIR and in the optical. Finally, in Section A3 we show the comparison of our black hole mass measurements.

A1 Emission and absorption lines' tables

In Table A1 are listed the emission lines present in the range 0.8–2.4 μm. Table A2 shows the absorption lines from which we measured the velocity dispersion using PPXF, while Table A3 shows the emission lines that we masked in the PPXF fitting procedure.

A2 Galaxy template fitting and velocity dispersion comparison

In Fig. A5, we show an example of the stellar velocity dispersion fit in the three wavelength regions (CaT, CO band-head in the *H* band and *K* band). We performed some tests to compare our velocity dispersion measurements in the different NIR wavelength ranges and with literature values (Fig. A7).

For the CO band-heads in the *K* band (2.255–2.400 μm), we compared the results obtained using the MIUSCATIR models and the GNIRS models (Fig. A6). The values of σ_* measured with the GNIRS models are systematically larger than the values measured with the MIUSCATIR models. However, the offset is quite small (13 km s^{-1}) and lies within the error bars. Thus, we conclude that the difference between the two libraries is negligible. We decided to use the MIUSCATIR models, since they have a larger wavelength coverage and they can be used also for the *H* band.

We also compared the σ_* measured from the CO band-heads in the *K* band (2.255–2.400 μm) and in the *H* band (1.57–1.72 μm). The values of $\sigma_{*,\mathrm{CO}}$ measured in the *H* and *K* bands are in good agreement. The offset (8 km s^{-1}) is within the measurement errors. We compared also the measurements from the CO band-heads and from the CaT. The results are in very good agreement, with a scatter around the one-to-one relation of 0.03 dex.

We compared our results with the σ_* values measured in the NIR by Riffel et al. (2015). They measured σ_* from the CO band-head in the *K* band and from the CaT for 48 galaxies, of which 13 are also in our sample. Our measurements of $\sigma_{*,\mathrm{CO}}$ in the *H* band are not in perfect agreement with the $\sigma_{*,\mathrm{CO}}$ and $\sigma_{*,\mathrm{CaT}}$ measured by Riffel et al. (2015). However, the scatter is quite small (0.06 dex) and the offset from the one-to-one relation (< 10 km s^{-1}) is comparable to the size of the error bars.

We compared our values of σ_* with the literature values measured from the optical absorption lines. The σ_* that we measured in the NIR is, on average, larger than the σ_* from the optical ($\sigma_{*,\mathrm{opt}}$). Fitting a one-to-one relation we found an offset of 33 km s^{-1}. We also compared the values of $\sigma_{*,\mathrm{CO}}$ with the values measured from the optical absorption lines (Ca H&K λλ3935, 3968 Å and Mg I λ5175 Å) from the BASS catalogue. The scatter is quite large and the values of $\sigma_{*,\mathrm{CO}}$ are larger on average than σ_* from the optical lines (offset = 18 km s^{-1}). These discrepancies can be due to different reasons. The size of the observed part of the galaxy from which the spectrum is extracted depends on the slit size and on the redshift on the galaxy. The σ_* measured in the nuclear region of the galaxy is larger than the σ_* measured in a larger region. The slit size used for our NIR observations is relatively small (0.8–1.5 arcsec) and this can cause our σ_* measurements to be larger than other measurements obtained using a larger slit. Another effect that can affect the σ_* measurements is the broadening of the absorption line due to the rotational motion of the stars. The absorption-line width includes components from both random motion and rotation and therefore the measured σ_* needs to be corrected for the rotation effect. Another possible explanation is that CO absorption lines probe the younger red supergiants, therefore $\sigma_{*,\mathrm{CO}}$ can be different from $\sigma_{*,\mathrm{opt}}$ if there is an age radial gradient in the stellar distribution (Rothberg & Fischer 2010; Rothberg et al. 2013). Kang et al. (2013) observed that $\sigma_{*,\mathrm{CO}}$ measured in the *H* band is in good agreement with the $\sigma_{*,\mathrm{opt}}$, based on a sample of 31 nearby galaxies. Riffel et al. (2015) instead found that $\sigma_{*,\mathrm{CO}}$ is on average smaller than $\sigma_{*,\mathrm{CaT}}$, whereas $\sigma_{*,\mathrm{CaT}}$ is in good agreement with $\sigma_{*,\mathrm{opt}}$.

A3 Black hole mass comparison

In this section, we compare our M_{BH} measurements from the broad Paβ line with M_{BH} measurements from the σ_*, and with values taken from literature. To calculate M_{BH} from the broad Paβ line, we used the formula from La Franca et al. (2015, equation 2), which is based on the FWHM and luminosity of Paβ. We considered also the formula from Kim et al. (2010):

$$\frac{M_{\mathrm{BH}}}{\mathrm{M}_\odot} = 10^{7.40} \left(\frac{L_{\mathrm{Pa}\,\beta}}{10^{42}\ \mathrm{erg\ s^{-1}}}\right)^{0.46\pm0.02} \left(\frac{\mathrm{FWHM}_{\mathrm{Pa}\,\beta}}{10^{3}\ \mathrm{km\ s^{-1}}}\right)^{1.41\pm0.09}. \quad \text{(A1)}$$

This relation has an intrinsic scatter on log M_{BH} of 0.27. Comparing the values obtained using these two relations (Fig. A8), we found an offset of 0.3 dex, which is small enough considering that the scatter of the relations is ∼0.2 dex. We compared also the M_{BH} derived from σ_{CO} and from the broad Paβ. The M_{BH} estimated from σ_{CO} are 1.1 dex larger than the values from Paβ.

We compared our results with the M_{BH} measured from reverberation mapping from 'The AGN Black Hole Mass Database'[2]

[2] http://www.astro.gsu.edu/AGNmass/

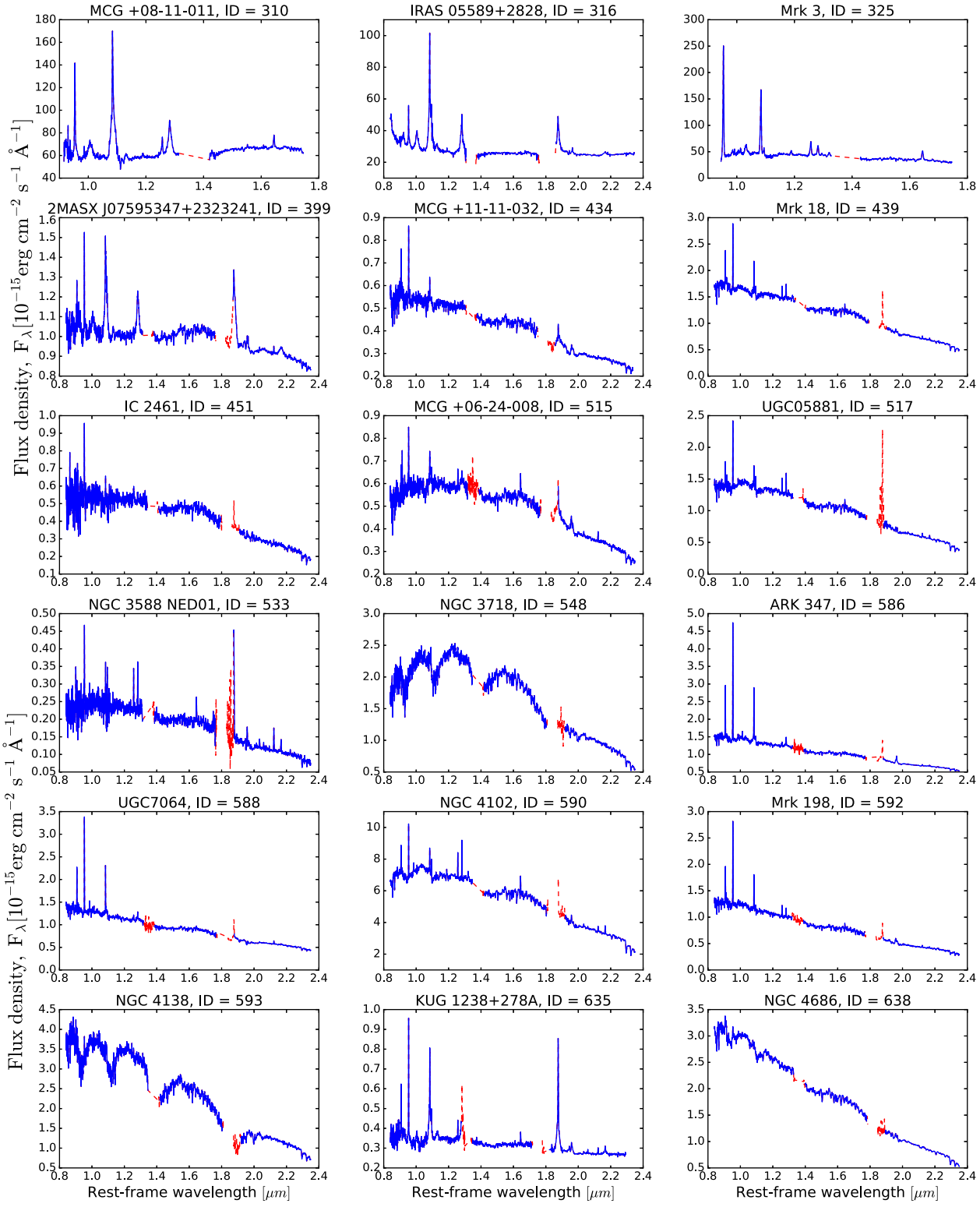

Figure A1. Galaxy spectra from new observations arranged in order of increasing ID (*Swift*/BAT 70-month hard X-ray survey ID – http://swift.gsfc.nasa.gov/results/bs70mon/). The red colour indicates regions of atmospheric absorption. Spectra are taken from the SpeX instrument on the IRTF with a 0.8-arcsec slit for all sources, except MCG +08-11-011 (ID = 310) and Mrk 3 (ID = 325), which were taken from the FLAMINGOS instrument on the Kitt Peak 4-m telescope with a 1.5-arcsec slit.

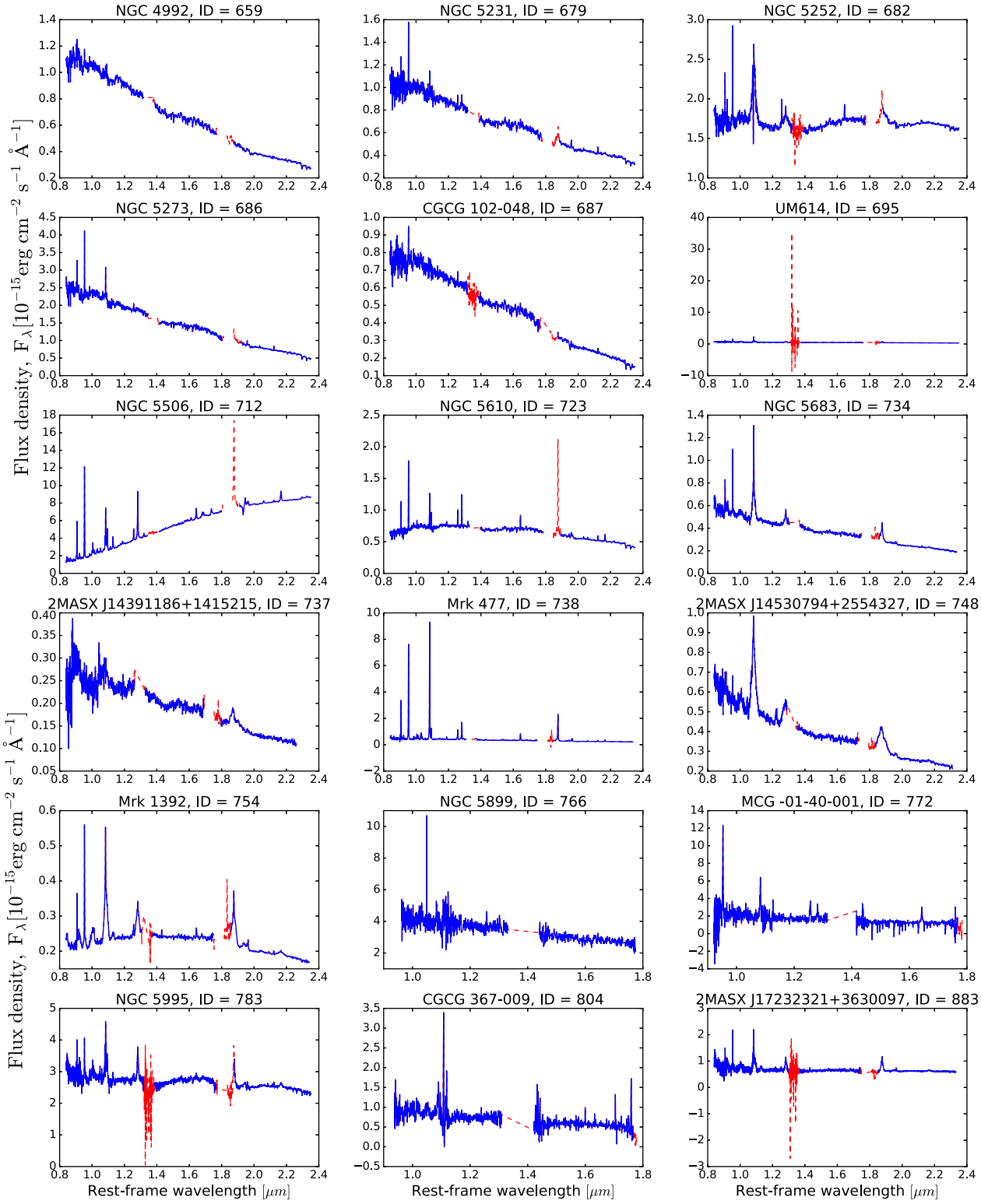

Figure A2. Galaxy spectra from new observations arranged in order of increasing ID (*Swift*/BAT 70-month hard X-ray survey ID – http://swift.gsfc.nasa.gov/results/bs70mon/). The red colour indicates regions of atmospheric absorption. Spectra are taken from the SpeX instrument on the IRTF with a 0.8-arcsec slit for all sources, except NGC 5899 (ID = 766), MCG -01-40-001 (ID = 772) and CGCG 367-009 (ID = 804), which were taken from the FLAMINGOS instrument on the Kitt Peak 4-m telescope with a 1.5-arcsec slit.

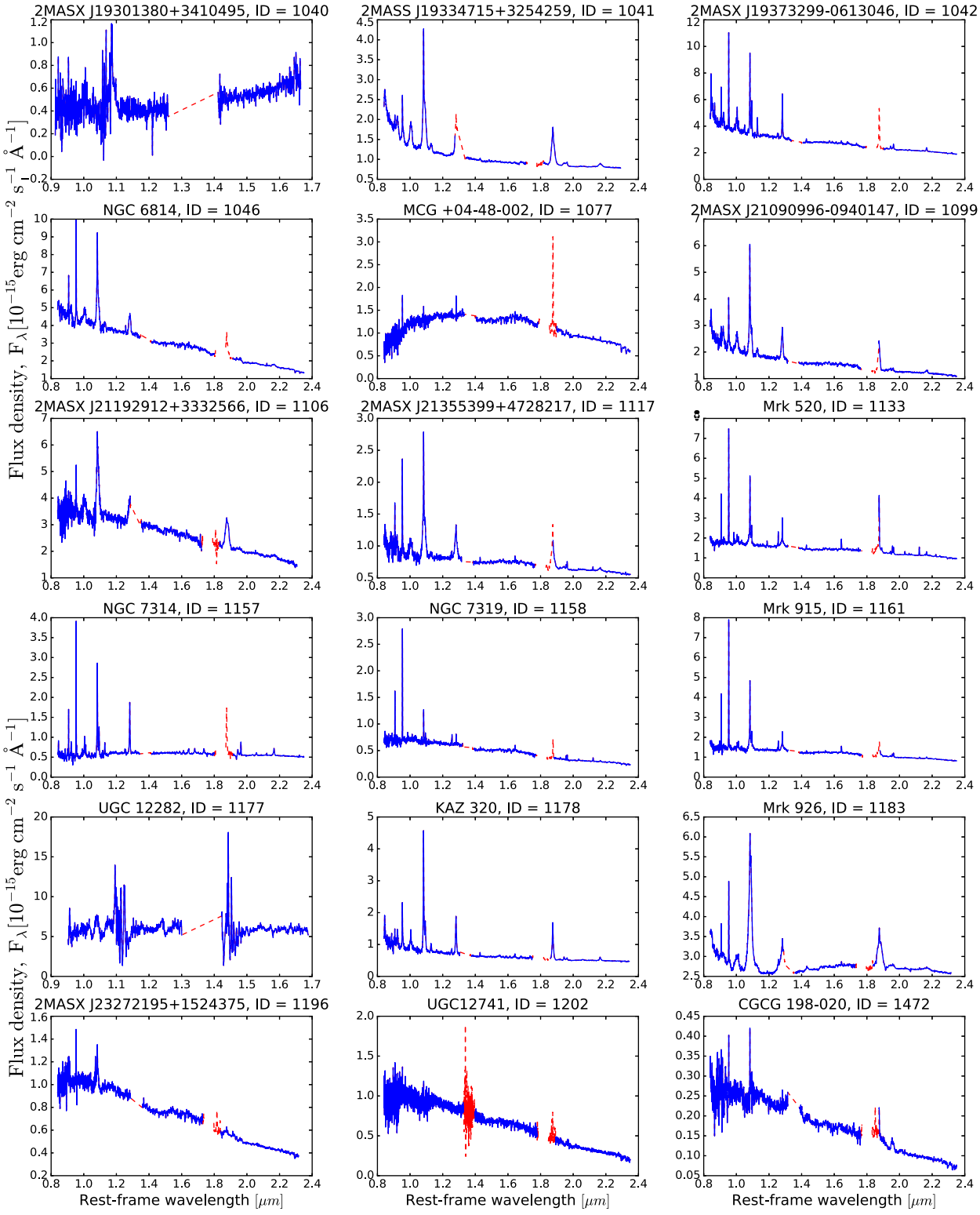

Figure A3. Galaxy spectra from new observations arranged in order of increasing ID (*Swift*/BAT 70-month hard X-ray survey ID – http://swift.gsfc.nasa.gov/results/bs70mon/). The red colour indicates regions of atmospheric absorption. Spectra are taken from the SpeX instrument on the IRTF with a 0.8-arcsec slit for all sources, except 2MASX J19301380+3410495 (ID = 1040) and UGC 12282 (ID = 1177), which were taken from the FLAMINGOS instrument on the Kitt Peak 4-m telescope with a 1.5-arcsec slit.

Table A1. Emission lines.

Emission line	Wavelength (μm)	Spectral region
O I	0.8449	Pa14
Pa16	0.8503	
Pa15	0.8545	
Pa14	0.8600	
Pa13	0.8665	
Pa12	0.8750	
Pa11	0.8863	
Pa10	0.9016	Paζ
[S III]	0.9069	
[Fe II]	0.9227	
Paζ	0.9229	
[S III]	0.9531	
Paϵ	0.9546	
[C I]	0.9827	Pa δ
[C I]	0.9853	
[S VIII]	0.9915	
[Fe II]	0.9999	
Paδ	1.0049	
He II λ4686	1.0126	
[S II]	1.0290	
[S II]	1.0320	
[S II]	1.0336	
[S II]	1.0370	
[N I]	1.0404	
[Fe II]	1.0500	Paγ
[Fe XIII]	1.0747	
He I	1.0830	
Paγ	1.0938	
[Fe II]	1.1126	
O I	1.1287	
He II λ4686	1.1620	Paβ
[P II]	1.1886	
[Ni II]	1.1910	
[S IX]	1.2520	
[Fe II]	1.2570	
[Fe II]	1.2788	
Paβ	1.2818	
[Fe II]	1.2950	
[Fe II]	1.3201	
[Si X]	1.4300	Br10
[Fe II]	1.5339	
[Fe II]	1.6436	
[Fe II]	1.6807	
Br11	1.6811	
Br10	1.7367	
Paα	1.8751	Paα
[Si XI]	1.9320	
Br δ	1.9446	
H_2	1.9564	
[Si VI]	1.9620	
H_2	2.0330	Brγ
[Al IX]	2.0400	
He I	2.0580	
H_2	2.1213	
Brγ	2.1655	
H_2	2.2227	
[Ca VIII]	2.3210	
H_2	2.2467	

Table A2. Absorption lines used in PPXF host galaxy fitting.

Absorption lines	Wavelength (μm)	Spectral region
Ca II	0.8498	CaT
Ca II	0.8542	CaT
Ca II	0.8662	CaT
CO (4–1)	1.5800	*H* band
CO (5–2)	1.6000	*H* band
CO (6–3)	1.6200	*H* band
CO (7–4)	1.6400	*H* band
CO (8–5)	1.6600	*H* band
^{12}CO (2–0)	2.2935	*K* band
^{12}CO (3–1)	2.3226	*K* band
^{13}CO (2–0)	2.3448	*K* band
^{12}CO (4–2)	2.3514	*K* band
^{12}CO (5–3)	2.3834	*K* band

Table A3. Emission lines masked in PPXF host galaxy fitting.

Emission line	Wavelength (μm)	Spectral region
Pa14	0.8598	CaT
[Fe II]	1.6436	CO *H* band
[Fe II]	1.6773	CO *H* band
Br11	1.6811	CO *H* band
[Ca VIII]	2.3210	CO *K* band

Table A4. CLs in the wavelength range 0.8–2.4 μm.

Coronal line	Wavelength (μm)	Ionization potential (eV)
[Ca VIII]	2.3210	127.7
[Si VI]	1.9620	166.8
[S VIII]	0.9915	280.9
[Al IX]	2.0400	284.6
[S IX]	1.2520	328.2
[Fe XIII]	1.0747	330.8
[Si X]	1.4300	351.1
[Si XI]	1.9320	401.4
[S XI]	1.9196	447.1

assuming a virial factor $\langle f \rangle = 5.5$ (Bentz & Katz 2015). We note that the relation from La Franca et al. (2015) was calibrated assuming a virial factor $f = 4.31$. We found a good agreement between $M_{\rm BH}$ from Paβ and the reverberation mapping values (average difference: 0.18 $\pm$ 0.03 dex). This is not surprising, since the relation from La Franca et al. (2015) was calibrated against the reverberation mapping $M_{\rm BH}$. For the $M_{\rm BH}$ from $\sigma_{\rm CO}$, we observe again that the $M_{\rm BH}$ measured from $\sigma_{\rm CO}$ seem to be overestimated.

For 43 AGN, we could compare our results with the $M_{\rm BH}$ values from the BASS catalogue. The $M_{\rm BH}$ from $\sigma_{*,\rm CO}$ are in agreement with the $M_{\rm BH}$ values from the optical σ_*, even if there is a large scatter (σ = 0.46 dex). There is an offset of 0.9 dex between the $M_{\rm BH}$ measured from $\sigma_{*,\rm CO}$ and $M_{\rm BH}$ measured from Hβ. The $M_{\rm BH}$ from Paβ are in good agreement with the values of $M_{\rm BH}$ measured from Hβ (offset = 0.1 dex, scatter = 0.3 dex), but not with $M_{\rm BH}$ measured from $\sigma_{*,\rm opt}$ (offset = 1.1 dex, scatter = 0.3 dex).

The $M_{\rm BH}$ calculated from the M–σ_* relation, using $\sigma_{*,\rm CO}$ or $\sigma_{*,\rm opt}$, agree with each other. In the same way, the measurements from broad lines, from single epoch Hβ or Paβ observations or from reverberation mapping, are in good agreement with each other.

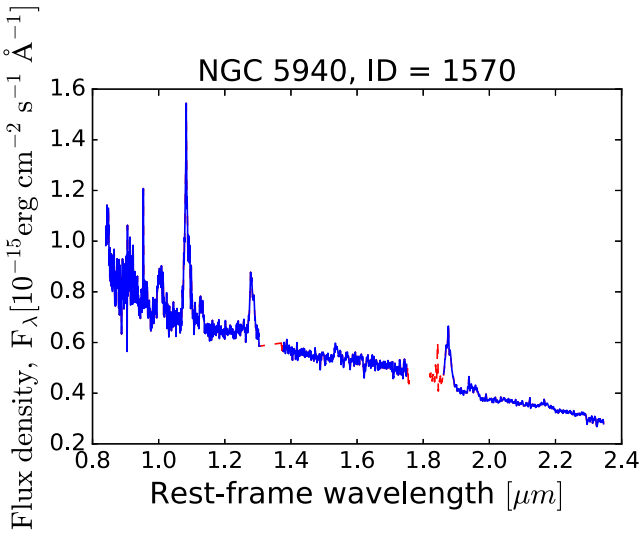

Figure A4. Galaxy spectra from new observations arranged in order of increasing ID (*Swift*/BAT 70-month hard X-ray survey ID – http://swift.gsfc.nasa.gov/results/bs70mon/). The red colour indicates regions of atmospheric absorption. This spectrum is taken from the SpeX instrument on the IRTF with a 0.8-arcsec slit.

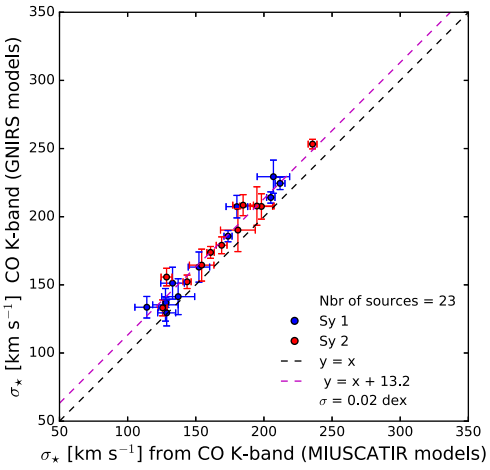

Figure A6. Comparison of σ_{*CO} measured in the *K*-band region using the MIUSCATIR models and the GNIRS models. The black dashed line shows the one-to-one relation ($x = y$) and the magenta dashed line shows the fit of a one-to-one relation allowing an offset.

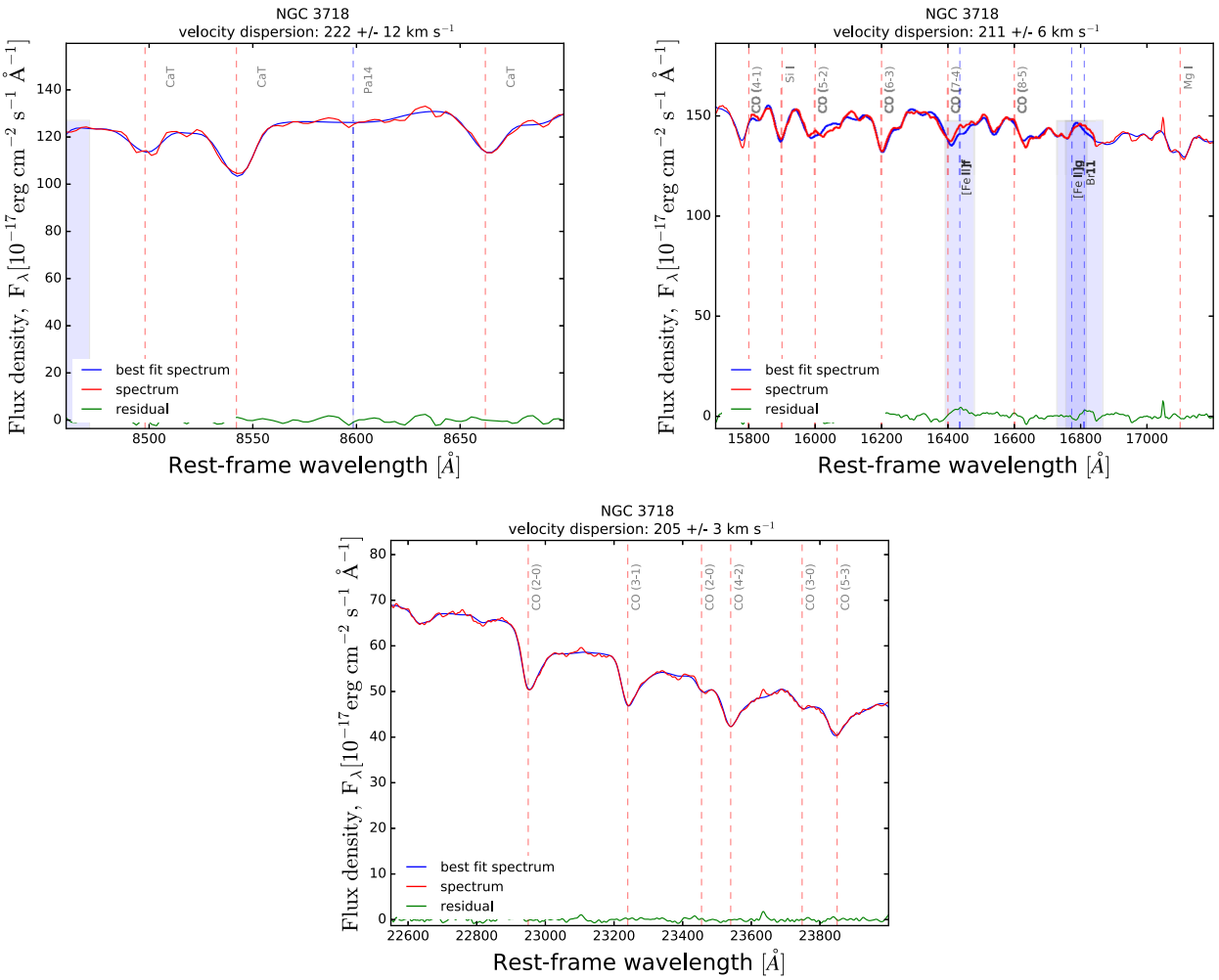

Figure A5. Example of PPXF fit of the CaT region (0.846–0.870 μm), CO band-head in the *H* band (1.570–1.720 μm) and in the *K* band (2.255–2.400 μm).

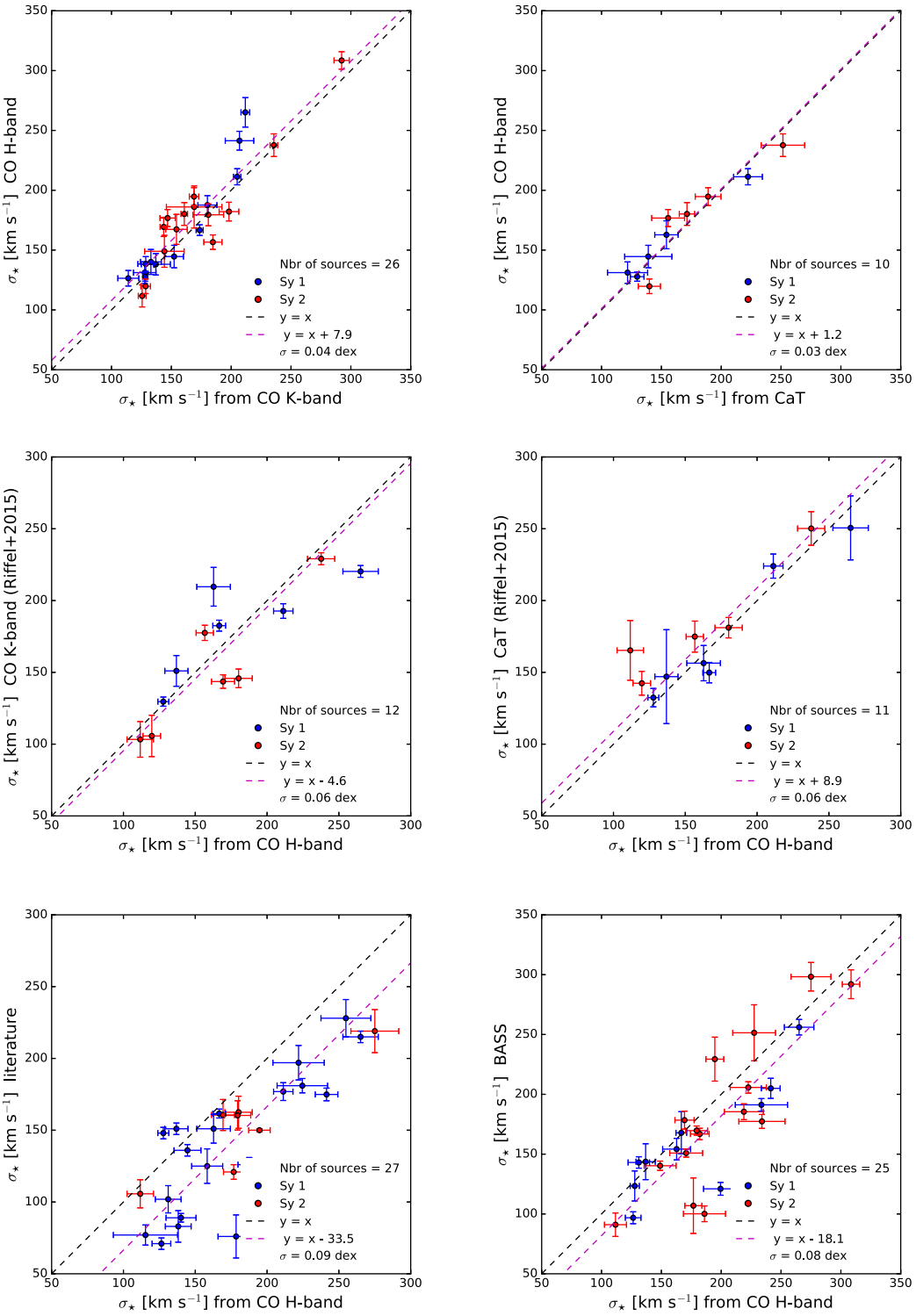

Figure A7. Comparison of velocity dispersion σ_* measurements. The black dashed line shows the one-to-one relation ($x = y$) and the magenta dashed line shows the fit of a one-to-one relation allowing an offset. Upper panels: comparison of $\sigma_{*,\mathrm{CO}}$ measured in the *K* band and in the *H* band (left) and comparison of $\sigma_{*,\mathrm{CO}}$ measured in the *H* band and $\sigma_{*,\mathrm{CaT}}$ (right). Middle panels: comparison of our $\sigma_{*,\mathrm{CO}}$ measured in the *H* band and the σ_* measured by Riffel et al. (2015) from the CO band-head in the *K* band (left) and from the CaT (right). Lower panels: comparison of $\sigma_{*,\mathrm{CO}}$ (*H* band) with literature values (left) and with the values of σ_* from the CaH and K and the MgIb absorption lines from the BASS catalogue (right).

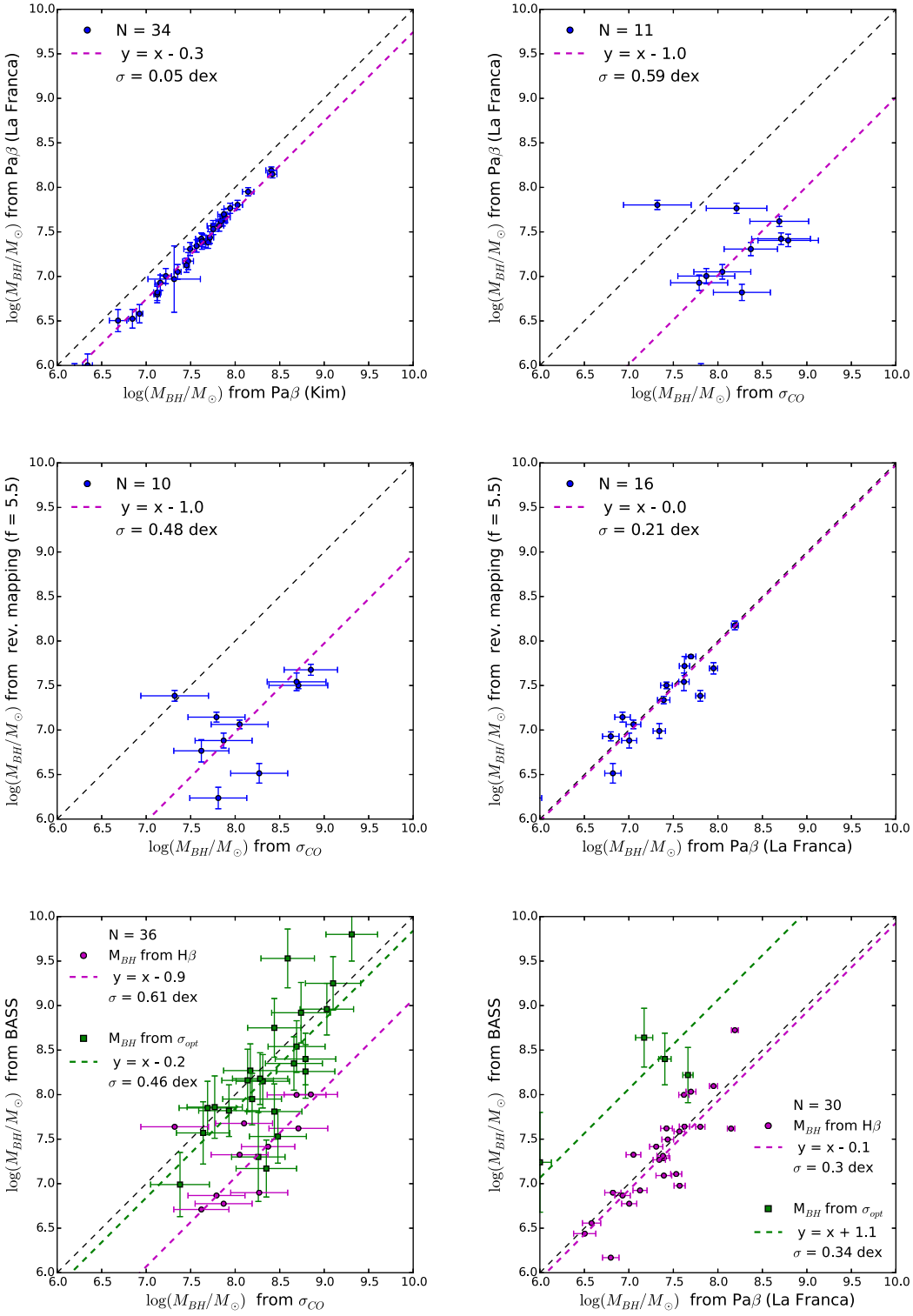

Figure A8. Comparison of $M_{\rm BH}$ measurements. The black dashed line shows the one-to-one relation and the magenta dashed line show the fit with a one-to-one relation allowing an offset. Upper panels: comparison of the $M_{\rm BH}$ estimated from broad Paβ with the prescriptions from Kim et al. (2010) and from La Franca et al. (2015, right). Comparison of the $M_{\rm BH}$ estimated from $\sigma_{*,\rm CO}$ and from broad Paβ with the prescriptions from La Franca et al. (2015, left). Middle panels: comparison of the $M_{\rm BH}$ estimated from $\sigma_{*,\rm CO}$ (left) and from broad Paβ (right) with the $M_{\rm BH}$ values from reverberation mapping (Bentz & Katz 2015). Lower panels: comparison of the $M_{\rm BH}$ estimated from $\sigma_{3,\rm CO}$ (left) and from broad Paβ (right) with the $M_{\rm BH}$ values from BASS. In green are the $M_{\rm BH}$ estimated from broad Hβ and in magenta the $M_{\rm BH}$ estimated from σ_* measured in the optical. The magenta and green dashed lines show the corresponding fit of a one-to-one relation allowing an offset.

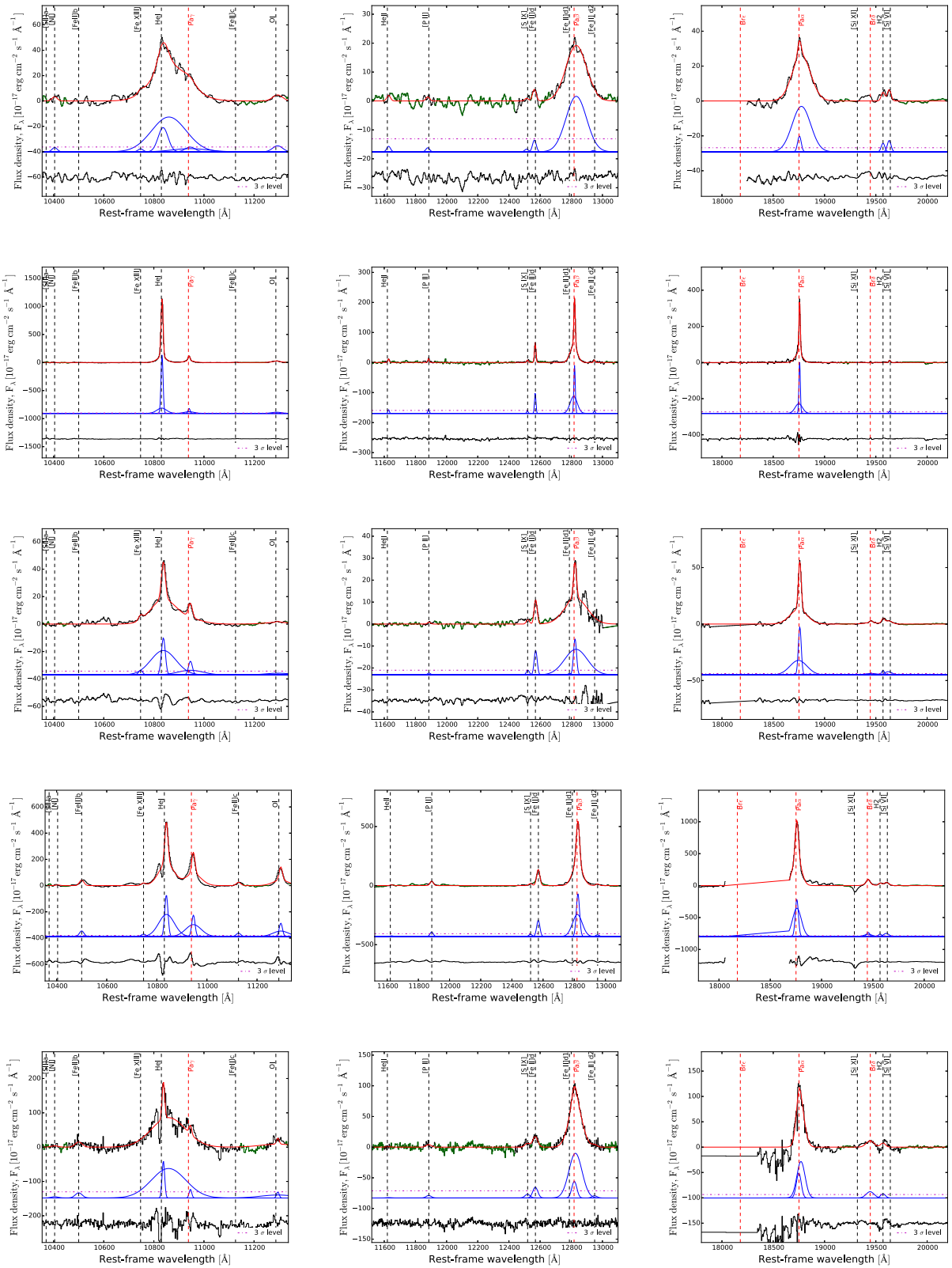

Figure A9. Fit of the He I λ1.0830 μm, Paβ and Paα regions for the Seyfert 1.9 and Seyfert 2 for which the broad Paβ was used to measure $M_{\rm BH}$. From the upper row: 2MASX J07595347+2323241, NGC 4395, KUG 1238+278A, NGC 5506 and NGC 5995. The best fit is in red, the model in blue and the residuals in black. The magenta dashed line in the middle part of the panels shows the detection threshold (S/N > 3) with respect to the fitting continuum (blue).

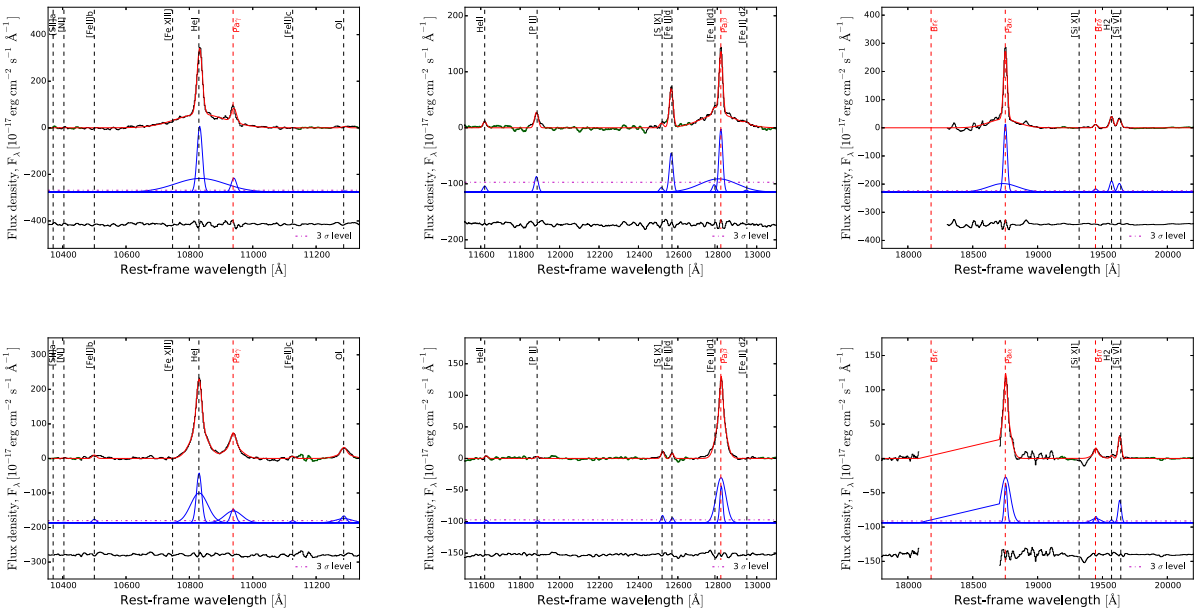

Figure A10. Fit of the He I λ1.0830 μm, Paβ and Paα regions for the Seyfert 1.9 and Seyfert 2 for which the broad Paβ was used to measure $M_{\rm BH}$. From the first row: Mrk 520 and NGC 7314. The best fit is in red, the model in blue and the residuals in black. In addition to the components explained above, the magenta dashed line in the middle part of the panels shows the detection threshold (S/N > 3) with respect to the fitting continuum (blue).

There is a significant offset of 0.9 dex between the values of $M_{\rm BH}$ derived using the M–σ_* relation and $M_{\rm BH}$ measured from the broad emission lines. Using the Gültekin et al. (2009) M–σ_* relation instead of Kormendy & Ho (2013) the offset is still 0.7 dex. We note that even the best virial mass estimators are known to suffer from systematic uncertainties of at least 0.3 dex (see, e.g., Shen 2013; Peterson 2014, and references therein) despite being tied to reproduce similar masses for systems where both are applicable (e.g. Graham et al. 2011; Woo et al. 2013). Another possibility might be that sources having both a black hole mass measurement and velocity dispersion are more likely to suffer residual AGN contamination in the host galaxy template that may bias the velocity dispersion. Further studies, such as using an integral field unit where the AGN and host galaxy emission can be separated and fit spacially as well as in wavelength space, are needed to fully understand this issue.

This paper has been typeset from a TEX/LATEX file prepared by the author.